

Setting Limits on GMSB Models using the $\gamma\gamma + \cancel{E}_T$ Final State¹

Eunsin Lee and Dave Toback

Texas A&M University

Ray Culbertson and Sasha Pronko

Fermilab

Max Goncharov

MIT

Abstract

We present the results of an optimized search for a gauge mediated supersymmetry breaking model with $\tilde{\chi}_1^0 \rightarrow \gamma\tilde{G}$ with $\tau(\tilde{\chi}_1^0) = 0$ ns in the $\gamma\gamma + \cancel{E}_T$ final state. We observe 0 events using 2.59 fb^{-1} of data collected by the CDF II detector, which is consistent with the background estimate of 1.23 ± 0.38 events. We set cross section and mass limits as well as interpret our results for lifetimes up to 2 ns in the $\tilde{\chi}_1^0$ lifetime vs. mass plane with a mass reach of $149 \text{ GeV}/c^2$ at $\tau(\tilde{\chi}_1^0) = 0$ ns.

¹This note supercedes the results in version 2.0 which was based on 2.0 fb^{-1} data and blessed on 11/06/2008. Differences are listed in an appendix. This note is now up to date and largely standalone.

Contents

1	Introduction	4
1.1	Theory and Phenomenology	4
1.2	Previous Searches	8
1.3	Overview of the Analysis	8
2	Triggers, Datasets and Object ID	10
2.1	Triggers and Datasets	10
2.2	Diphoton Samples and Object ID	10
3	Backgrounds	15
3.1	Overview	15
3.2	QCD Backgrounds with Fake \cancel{E}_T	15
3.2.1	QCD Background due to Energy Mismeasurements in the Calorimeter	15
3.2.2	Fake \cancel{E}_T from QCD with Events Reconstruction Pathologies	16
3.3	Electroweak Backgrounds with Real \cancel{E}_T	20
3.3.1	Charged Leptonic Decay Channels	20
3.3.2	Neutral Leptonic Decay Channels	21
3.4	Non-Collision Events	23
3.4.1	Beam Halo Events	23
3.4.2	Cosmic Ray Events	26
3.5	Background Summary	31
4	Acceptances for GMSB Models	32
5	Estimation of the Systematic Uncertainties	33
5.1	Acceptance Uncertainties	33
5.1.1	Photon ID and Isolation Efficiencies	33
5.1.2	ISR/FSR (Initial and Final State Radiation)	34
5.1.3	JES (Jet Energy Scale)	34
5.1.4	\cancel{E}_T Significance parameterization and calibration	34
5.1.5	PDFs (Structure Functions)	34
5.2	Production Cross Section Uncertainties	34
5.2.1	PDFs (Structure Functions)	35
5.2.2	Q^2 (Renormalization Scale)	35
5.3	Summary of the Systematic Uncertainties	35
6	Optimization and Expected Limits	36

7 Data, Cross Section Limits and Final Results	42
7.1 The Data and Cross Section Limits	42
7.2 The GMSB Exclusion Region	42
8 Conclusions and Prospects for the Future	45
A Appendix-I: Changes Since the $2\text{ }fb^{-1}$ Analysis	46
B Appendix-II: PRL Figures	47
C Appendix-III: Details of Large fake \cancel{E}_T from Pathologies	50
C.1 Fake \cancel{E}_T from Picking the Wrong Vertex	50
C.2 Tri-Photon Events with a Lost Photon	50

1 Introduction

The $\gamma\gamma + \cancel{E}_T$ final state is present in many theoretical models of new physics beyond the Standard Model (SM) [1]. The most commonly discussed theory that would produce it is gauge mediated supersymmetry breaking (GMSB) [2] with $\tilde{\chi}_1^0 \rightarrow \gamma\tilde{G}$ where the $\tilde{\chi}_1^0$ is the lightest neutralino and the next-to-lightest supersymmetric particle (NLSP), and the \tilde{G} is the supersymmetric partner of the graviton, the gravitino, and the lightest supersymmetric particle (LSP). GMSB models are compelling for both theoretical and experimental reasons [3]. As the messenger interactions are flavor-independent it intrinsically suppresses flavor-changing neutral currents and CP-violating processes to SM levels. It is also consistent with cosmological constraints [4] as all SUSY particles produced in the early universe decay to the \tilde{G} LSP, which can be a warm dark matter candidate, depending on the mass of the \tilde{G} [5]. Finally, for much of the parameter space this model naturally predicts $\tilde{\chi}_1^0 \rightarrow \gamma\tilde{G}$ which produces high energy photon events at the Tevatron and gained favor with the appearance of the $ee\gamma\gamma\cancel{E}_T$ candidate event in Run I [6].

For these models current limits from collider experiments, astronomy and cosmology favor a heavy $\tilde{\chi}_1^0$, with a mass on the order of ~ 100 GeV and a lifetime on the order of nanoseconds that decays to $\gamma\tilde{G}$ [5]. These limits restrict the masses of the squarks and gluons to be so large that they are too heavy to be produced at the Tevatron, thus gaugino pair-production channels dominate [2]. In this case the decays produce a pair of $\tilde{\chi}_1^0$'s in association with other particles, with each $\tilde{\chi}_1^0$ decaying into a \tilde{G} , that gives rise to \cancel{E}_T , and a photon. Depending on how many of the two $\tilde{\chi}_1^0$'s decay inside the detector, due to their large decay length, the event has the signature $\gamma\gamma + \cancel{E}_T$, $\gamma + \cancel{E}_T$ or \cancel{E}_T with one or more additional high E_T particles. At CDF we separate the search for GMSB into short lifetime searches ($\tau < 2$ ns) and long lifetime searches, following the recommendations of Ref [7]. Large lifetime searches in the delayed $\gamma + \cancel{E}_T + jet$ final state are described in [8]. In this note we focus on the optimization of the $\gamma\gamma + \cancel{E}_T$ final state, which is more sensitive to lower $\tilde{\chi}_1^0$ lifetimes which are favored for the large $\tilde{\chi}_1^0$ masses [7].

The structure of this note is as follows: This section continues with a description of GMSB models in more detail, summarizes the previous searches and provides an overview of our analysis and search strategy. Section 2 describes the dataset and the preselection. Section 3 outlines the different backgrounds and how we estimate them for use in the optimization procedure. Section 4 describes the Monte Carlo (MC) that we use to model the signal acceptance and Section 5 gives the systematic uncertainties on the acceptance and the production cross sections. The optimization procedure, and its result, are given in Sec. 6. We unblind the signal region in Sec. 7, compare with expectations and set cross section, mass and lifetime limits. We conclude in Sec. 8 with expectations for the future.

This is a revised note that supercedes the blessed (November 06, 2008) results based on 2.0 fb^{-1} data. Appendix A lists the changes to the analysis since the blessing. This version of the note contains the current status of the analysis and is largely standalone; all the numbers are up to date. Appendix B contains the versions of the figures for the PRL [9].

1.1 Theory and Phenomenology

Supersymmetric models with GMSB provide an interesting alternative to the scenario in which the soft terms of the low-energy fields are induced by gravity [2]. These theories allow for a natural suppression of flavor violations in the supersymmetric sector and have very distinctive phenomenological features. In GMSB models the standard model gauge interactions act as the messengers of supersymmetry breaking if fields within the supersymmetry breaking sector transform

Λ	the effective SUSY breaking scale
M_m	the messenger mass scale
N	the number of messenger fields
$\tan\beta$	the ratio of the MSSM Higgs vacuum expectation values
$\text{sign}(\mu)$	the sign of the Higgs sector mixing parameter
$C_{\tilde{G}}$	the \tilde{G} mass factor

Table 1: The 6 parameters of the minimal model of GMSB.

under the standard model gauge group.

The minimal model of GMSB can be described in terms of the 6 free parameters listed in Table 1 [10]. The effective SUSY breaking scale, Λ , is important because it sets the overall mass scale of the supersymmetric particles. To first approximation, all of the MSSM superpartner masses scale linearly with Λ . The number of messenger fields, N , is also very important because it determines which sparticle is the NLSP. In these models the NLSP is either the stau, $\tilde{\tau}$, or the $\tilde{\chi}_1^0$ depending on parameter choice [10]. For $N = 1$ the NLSP is mainly the lightest neutralino, and for $N \geq 2$ it is one of the sleptons. We will focus on the $\tilde{\chi}_1^0$ -NLSP case here, for which the branching ratio is $\sim 100\%$ to decay to a photon and a \tilde{G} . While the NLSP lifetime scales like the gravitino scale factor, $C_{\tilde{G}}$, squared as well as $M_{\tilde{G}}$ [2], for much of the parameter space it is of the order of ns. The mass range $M_{\tilde{G}}$ between a few hundred eV/c² and a few keV/c² is favored for cosmological reasons and typically produces a neutralino lifetime of less than a few hundred ns depending on the NLSP mass [5]. This parameter is important for our purposes because the lifetime determines whether the NLSP decays inside or outside the detector. For more discussion of the issues and details of prospects of searches with long-lived neutralinos-NLSPs which decay to $\gamma\tilde{G}$ see Ref. [7].

As there are many GMSB parameter combinations that match this phenomenology, representative “model lines” have been identified that cover specific characteristics of GMSB models with an $\tilde{\chi}_1^0$ NLSP with only one free parameter setting the particle masses. We choose the most commonly used for this analysis, the Snowmass Points and Slopes (SPS) model line 8 [10]: $N = 1$; $M_m/\Lambda = 2$; $\tan\beta = 15$; and $\mu > 0$, where Λ is a free parameter. We also take $C_{\tilde{G}}$ as a free parameter as it controls the \tilde{G} mass. Taking these two model parameters is the equivalent of taking the $\tilde{\chi}_1^0$ mass, $m_{\tilde{\chi}_1^0}$, and lifetime, $\tau_{\tilde{\chi}_1^0}$, as free parameters. As shown in Ref. [2] we have the relationship

$$\tau_{\tilde{\chi}_1^0} = C \cdot \left(\frac{100 \text{ GeV}}{m_{\tilde{\chi}_1^0}} \right)^5 \cdot \left(\frac{m_{\tilde{G}}}{1 \text{ keV}} \right)^2 \text{ ns} \quad (1)$$

where $C = 69.33$, with $m_{\tilde{G}}$ in keV and $m_{\tilde{\chi}_1^0}$ in GeV. We will describe our analysis in terms of these two variables for clarity of presentation.

For this model at the Tevatron $\tilde{\chi}_1^0$ ’s are mostly pair produced as end products of cascade decays from a chargino, $\tilde{\chi}_1^\pm$, pair ($\sim 45\%$ of all channels) or a $\tilde{\chi}_1^\pm$ and a $\tilde{\chi}_2^0$ ($\sim 25\%$ of all channels) [14]. The major decay channels are shown in Fig. 1. Table 2 gives some example GMSB model parameters, the resulting $\tilde{\chi}_1^0$ masses and lifetimes, and the next-to-leading-order (NLO) production cross sections for our region of interest. The production cross sections are calculated to leading-order using PYTHIA [11] with the NLO corrections using the k-factors shown in Figure 2 as a function of $\tilde{\chi}_1^0$ masses for $\tilde{\chi}_1^\pm$ pair and $\tilde{\chi}_1^\pm\tilde{\chi}_2^0$ production as taken from [12]. The values range between 1.1-1.3 for the mass range considered. The production cross section is independent of the $\tilde{\chi}_1^0$ lifetime, as this only scales with the \tilde{G} mass for a fixed $\tilde{\chi}_1^0$ mass [2]. We use production from all process to estimate

our sensitivity as it produces the best sensitivity to the model [13].

Since astronomy constraints restrict the gravitino mass, $m_{\tilde{G}}$, to cover near a keV/c^2 [5], for much of the parameter space the $\tilde{\chi}_1^0$ can be long-lived from Eq. (1), with a decay time on the order of nanoseconds which corresponds to decay lengths of meters. The $\tilde{\chi}_1^0$ can decay inside the detector or, in a fraction of cases, leave the detector volume before it decays. This separates the following event signatures: $\gamma\gamma + \cancel{E}_T$, $\gamma + \cancel{E}_T$ or \cancel{E}_T , each in association with jets from the τ 's in the cascade decays. In this note we will focus on the $\gamma\gamma + \cancel{E}_T$ case as this is more sensitive to low lifetimes, on the order of nanoseconds (< 2 ns), which is favored for large masses for cosmology regions [7]. While we will take advantage of the other high energy final state particles produced from the decays, we retain a model independent type analysis by not explicitly requiring the identification of taus. Next we outline our search strategy and the datasets.

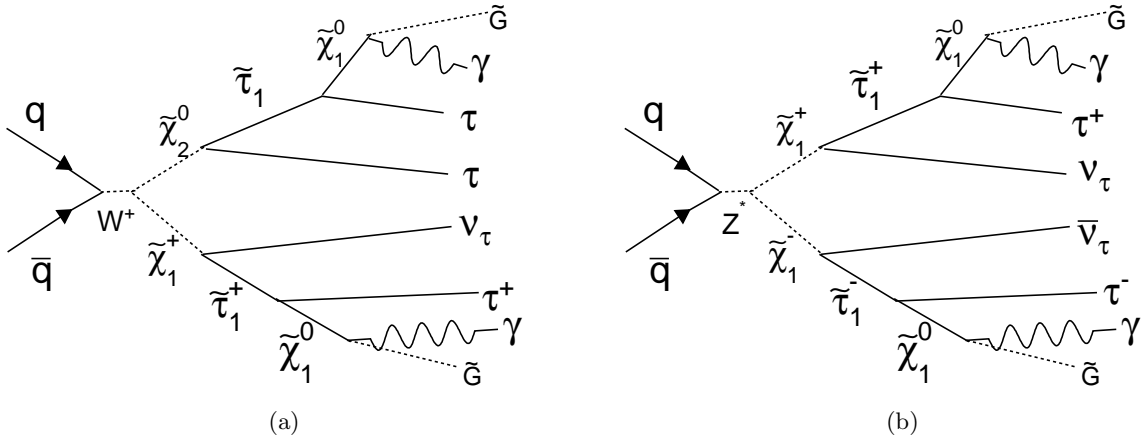


Figure 1: Feynman diagrams of the dominant tree production processes at the Tevatron for the GMSB model line we consider: $\tilde{\chi}_1^{\pm}\tilde{\chi}_2^0$ (45%) (a) and $\tilde{\chi}_1^{\pm}$ pair (25%). Note that we only show one choice for the charge. The remaining processes are slepton (τ_1 , e_R , μ_R) pair production.

$m_{\tilde{\chi}_1^0}$ (GeV/c 2)	$\tau_{\tilde{\chi}_1^0}$ (ns)	$m_{\tilde{G}}$ (eV/c 2)	Λ (TeV)	k-factor	NLO σ_{prod} (fb)
70	0	1.38	53.5	1.23	999.9
90	0	2.18	67.2	1.20	286.8
100	0	2.63	74.0	1.19	169.0
130	0	4.34	95.0	1.16	36.23
130	2	317	95.0	1.16	36.23
140	0	4.99	101.8	1.15	22.97
150	0	5.7	108.8	1.14	14.54

Table 2: Examples of $\tilde{\chi}_1^0$ masses and lifetimes relevant for this analysis and their translation to the SUSY parameters in accordance with the GMSB Snowmass Slope SPS 8 [10]. Also given are the NLO production cross sections. Note that the production cross section is independent of the $\tilde{\chi}_1^0$ lifetime. Also note that since we are not yet sensitive to the cosmology favored region, $m_{\tilde{G}} \approx 1$ keV, we are focusing on $\tau_{\tilde{\chi}_1^0} = 0$ cases.

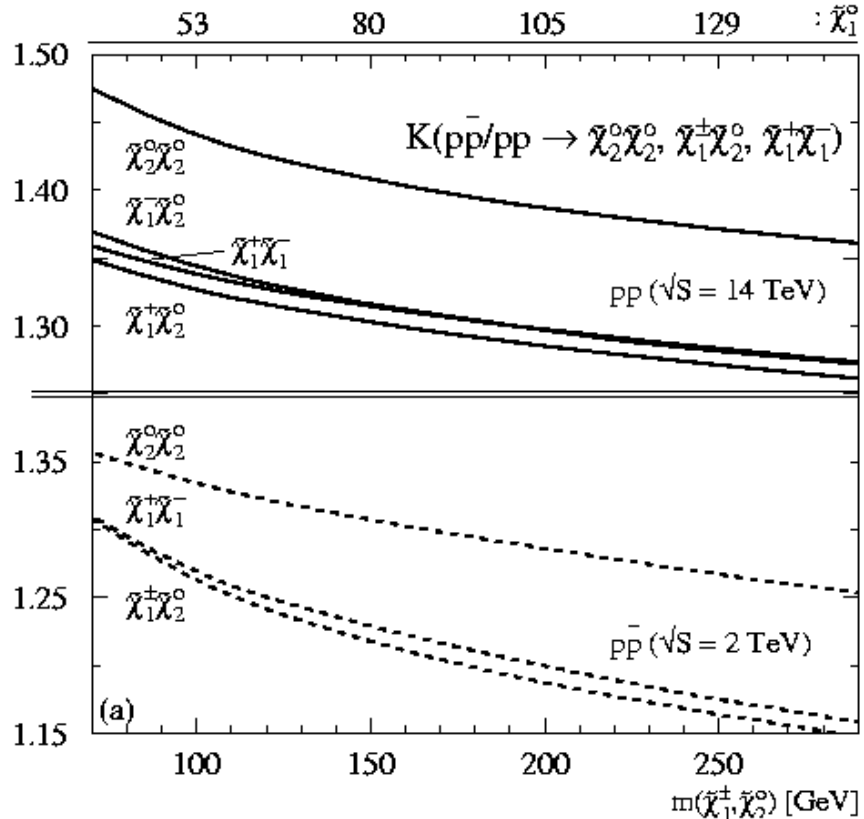


Figure 2: The k-factors for use in modifying the LO production cross sections of $\tilde{\chi}_1^\pm$ pair and $\tilde{\chi}_1^\pm \tilde{\chi}_1^0$ production as a function of the average mass of the $\tilde{\chi}_1^\pm$ and $\tilde{\chi}_2^0$ which are almost identical in the scenario chosen in Ref. [10]. The figure is taken from Fig. 3a of Ref. [12]. For convenience the $\tilde{\chi}_1^0$ mass is plotted as a second x-axis, taken from Fig. 3b therein.

1.2 Previous Searches

There have been many previous searches for anomalous $\gamma\gamma + \cancel{E}_T$ production including Run I searches from CDF [6] and DØ [15] and multiple searches from LEP II [16]. The most recent search from CDF in the $\gamma\gamma + \cancel{E}_T$ final state at CDF was with 202 pb^{-1} of data and was published in 2004 [17]. With zero observed events with $\cancel{E}_T > 45 \text{ GeV}$ on a background of 0.27 ± 0.12 and an 18% systematic error we set a 3.3 event 95% C.L. upper limit on the expected number of signal events. Using the NLO predictions we set a limit of $M_{\tilde{\chi}_1^0} > 93 \text{ GeV}/c^2$, assuming the $\tilde{\chi}_1^0$ lifetime is zero. The current most sensitive search for GMSB with $\tau = 0$ is from DØ using 1.1 fb^{-1} of data [18]. The observed upper limits are $M_{\tilde{\chi}_1^0} > 125 \text{ GeV}/c^2$.

In 2006 a CDF search [19] for a single photon with delayed arrival time, using the EMTiming system [20], at least one jet, and \cancel{E}_T , set the most stringent limits on GMSB for nanosecond lifetimes and large masses of the $\tilde{\chi}_1^0$'s. The search found 2 events using 570 pb^{-1} of data, which was consistent with the background estimate of 1.3 ± 0.7 events. Figure 3 shows the exclusion region in the $\tilde{\chi}_1^0$ lifetime vs. mass plane with a mass reach of $101 \text{ GeV}/c^2$ at $\tau_{\tilde{\chi}_1^0} \sim 5 \text{ ns}$. This results extended the world sensitivity to these models beyond those from LEP II, which searched for non-zero $\tilde{\chi}_1^0$ lifetimes using photon pointing [16].

1.3 Overview of the Analysis

This analysis is designed to extend the sensitivity to GMSB models in the $\gamma\gamma + \cancel{E}_T$ final state with $\tau = 0$ and to estimate our sensitivity for $\tau < 2 \text{ ns}$. Our search is designed to identify the $\gamma\gamma + \cancel{E}_T$ events from the cascade decays from $\tilde{\chi}_1^\pm$ and/or $\tilde{\chi}_2^0$. The new features of our analysis since the last $\gamma\gamma + \cancel{E}_T$ search with 202 pb^{-1} are the following:

- Use the EMTiming system [20] to reject cosmic rays and beam halo backgrounds.
- Use a new *Met Resolution Model* [21] to improve QCD background rejection.
- Simplify and re-optimize the analysis due to more direct ways of rejecting backgrounds.
- Use 13 times the data (2.6 fb^{-1}).
- Estimate the sensitivity to non-zero lifetimes.

We examine events with two isolated, central ($|\eta| \lesssim 1.0$) photons with $E_T > 13 \text{ GeV}$ for the presence of significant \cancel{E}_T . All candidates are required to pass global event selection, photon ID and isolation requirements, and pass non-collision background rejection requirements. This set of cuts defines our preselection sample. The final signal region is defined by further kinematic cuts selected to optimize the rejection of the remaining backgrounds while retaining acceptance for our signal. The dominant backgrounds are QCD events ($\gamma\gamma, \gamma - \text{jet} \rightarrow \gamma\gamma_{\text{fake}}$ and $\text{jet} - \text{jet} \rightarrow \gamma_{\text{fake}}\gamma_{\text{fake}}$) with fake \cancel{E}_T due to energy mis-measurement, electroweak events with real \cancel{E}_T (e.g., $W\gamma \rightarrow e\nu\gamma \rightarrow \nu\gamma_{\text{fake}}\gamma$), and non-collision backgrounds such as PMT spikes, cosmic rays, and beam-halo (B.H.) interactions.

We perform an *a priori* analysis in the sense that we blind the signal region and select the final event requirements based on the signal and background expectations alone. In Section 6 we optimize our predicted sensitivity using a simulation of our GMSB model (see Section 4) and calculate, for each GMSB parameter point, the lowest expected 95% C.L. cross section limit as a function of the following event variables: \cancel{E}_T Significance, H_T and $\Delta\phi(\gamma_1, \gamma_2)$, where H_T is defined

as the sum of E_T of the two photons, any jets with $E_T > 15$ GeV and $|\eta| < 2.4$, and the \cancel{E}_T . After this procedure we are left with an optimal, robust set of requirements that define the signal region.

In addition to setting limits on $\tau = 0$ decays, we investigate our sensitivity for the lifetime region $\tau < 2$ ns to complement the delayed photon analysis [19]. As shown in Figure 3 there is an uncovered region below about a ns.

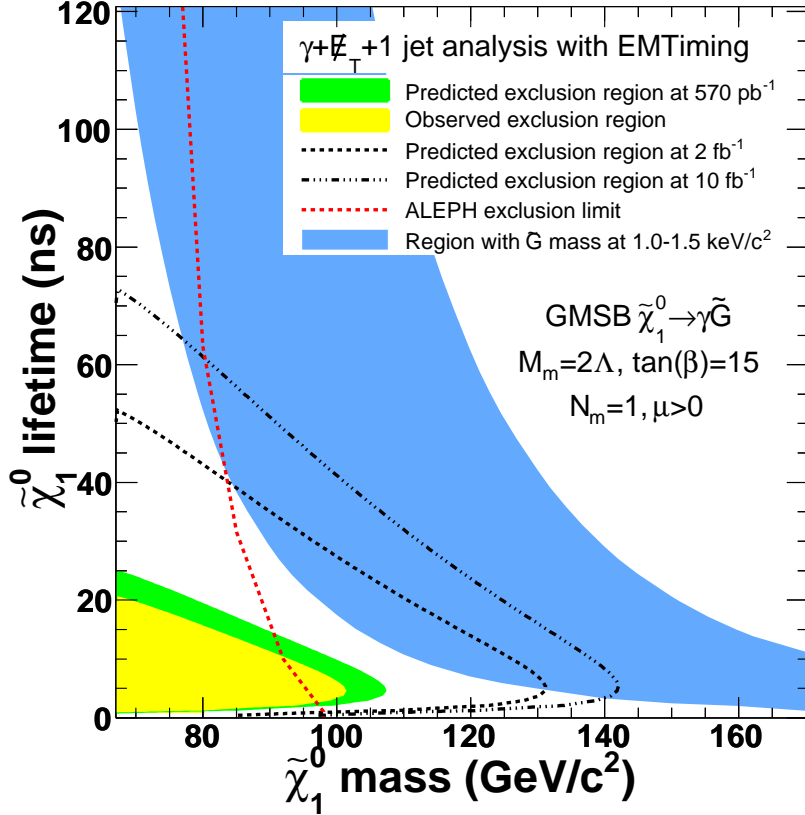


Figure 3: The predicted and observed exclusion region from the delayed photon search in the $\gamma + \cancel{E}_T + \text{jet}$ final state, taken from Ref. [19], along with cosmology favored region and the exclusion limit from ALEPH/LEP [16]. Note that we fixed for the incorrect cosmology favored region as described in Section A. Appendix-I.

2 Triggers, Datasets and Object ID

In this section we describe the trigger, dataset, and the object ID used to create the preselection sample. The analysis is based on data collected from the beginning of Run II starting with run 190851 (December 7, 2004), after the EMTiming system became available, and up to run 261005 (April 16, 2008). The integrated luminosity is obtained from the offline database and is scaled by the standard 1.019 correction factor [22]. To ensure the quality of data, the good run list v.23 [23] for the *Photon* group is applied. It requires good CAL, SMX, COT (COT degraded period is allowed, but Silicon is required during that period). After all requirements we are left with $2.59 \pm 0.16 \text{ fb}^{-1}$ of data [24] for periods 1 to 17.

To get the preselection sample we select a set of events that pass the photon triggers, photon ID and isolation, phoenix rejection, vertex requirements and re-assignment (vertex swap), non-collision removal cuts, and \cancel{E}_T cleanup cuts, all given in Tables 3-8. At the end we are left with a sample of 38,053 events, as described in Table 9. Next we describe each of the cuts in detail.

2.1 Triggers and Datasets

The events used in this analysis are required to pass one of the DIPHOTON_12 (iso), DIPHOTON_18 (no-iso), PHO_50 (no-iso) or PHO_70 (no-hadem) triggers[25]. The PHO_50 and PHO_70 triggers are added to recover potential loss in efficiency for χ^2_{CES} at high photon E_T [26]. The requirements for each at the three trigger levels are listed in Table 3. The $\gamma\gamma + X$ data are “ntuplized” in the “cdfpstn:cdipad,h,i,j” Stntuples. We use the Stntuple dev_243 [27] and version 6.1.4 of the cdfsoft2 release.

2.2 Diphoton Samples and Object ID

Diphoton candidate events are selected from the sub-sample of events that pass one of the triggers. Both leading photons are required to be in the central, $|\eta| \leq 1.1$, have $E_T^\gamma > 13 \text{ GeV}$, and pass the standard photon ID and isolation requirements, with two additional ID requirements. We take the trigger efficiency to be 100% for these cuts [28]. The full set of ID and isolation requirements are given in Table 4.

In addition to the standard photon ID and isolation cuts [29] we have added two additional cuts to suppress both $e\gamma$ events where an electron fakes a prompt photon [30] and fake photons from PMT spikes [31]. Since an important source of background with large real \cancel{E}_T is $e\gamma + X \rightarrow \gamma\gamma_{fake} + X$ events where an electron fakes a prompt photon we have added Phoenix rejection cuts [30] to the list of photon ID cuts. In many cases such a photon is either due to a bremsstrahlung in the detector material in front of the COT or due to a lost track (see Ref. [30] for details). These electrons usually leave a few silicon hits and can be reconstructed by the Phoenix tracking algorithm. To reduce contamination by $e\gamma$ events, we reject events if either photon is matched to a Phoenix track. PMT spikes in the CEM calorimeter can produce a fake photon signature and give fake \cancel{E}_T . To suppress this background, we remove events with a large PMT asymmetry: $A = |pmt1 - pmt2|/(pmt1 + pmt2)$, where $pmt1$ and $pmt2$ are the energies reported from PMT-1 and PMT-2, respectively.

All events are required to pass a set of global requirements. To help maintain the projective nature of the calorimeter we select events with at least one vertex of class 12 with $|Z_{vx}| \leq 60 \text{ cm}$. The E_T of all calorimeter objects (individual towers, photons, electrons, jets and \cancel{E}_T) are calculated with respect to the highest $\sum P_T$ vertex. However, in some events our algorithm chooses the wrong primary interaction vertex, for example, when a $\gamma\gamma$ pair is produced by one interaction and overlaps

DIPHOTON_12	
L1	Single tower $E_T > 8$ GeV ($z = 0$) Single tower Had/EM < 0.125 unless $E_T > 14$
L2	Two high E_T pass clusters, $E_T > 10$ ($z = 0$), $\eta < 3.6$ Both clusters Had/EM < 0.125 Both clusters Iso < 3 Iso < 0.15 E_T
L3	Two L3 clusters, $E_T > 12$ ($z = 0$) Both clusters Had/EM < 0.055 + 0.00045 E $E_T > 200$ Both clusters Iso(cone 0.4) < 2 < 0.10 E_T for central, average and scaled CES $\chi^2 < 20$
DIPHOTON_18	
L1	Single tower $E_T > 8$ GeV ($z = 0$) Single tower Had/EM < 0.125 unless $E_T > 14$
L2	Two high E_T pass clusters, $E_T > 16$ ($z = 0$), $\eta < 3.6$ Both clusters Had/EM < 0.125
L3	Two L3 clusters, $E_T > 18$ ($z = 0$) Both clusters Had/EM < 0.055 + 0.00045 E $E_T > 200$ for central, average and scaled CES $\chi^2 < 20$
PHO_50	
L1	Single tower $E_T > 8$ GeV ($z = 0$) Single tower Had/EM < 0.125 unless $E_T > 14$
L2	$E_T > 40$ GeV Had/EM < 0.125
L3	$E_T > 50$ GeV Had/EM < 0.125 (off at 200 GeV)
PHO_70	
L1	Single tower EM+Had $E_T > 10$ GeV ($z = 0$) Single tower Had/EM < 0.125 unless $E_T > 14$
L2	$E_T > 70$ GeV
L3	$E_T > 70$ GeV Had/EM < 0.2 + 0.001 E , removed at $E = 100$ GeV)

Table 3: The triggers used to create the diphoton sample. PHO_50 and PHO_70 are added to the standard diphoton triggers to recover loss in efficiency of χ^2_{CES} at high E_T^γ . We only require an event to pass one of these triggers. Since we require two isolated central photons with $E_T > 13$ GeV we take the trigger efficiency for our analysis to be 100%.

The Standard Photon ID and Isolation Cuts	
detector	CEM
corrected E_T	≥ 13 GeV
CES fiduciality	$ X_{CES} \leq 21$ cm $9 \text{ cm} \leq Z_{CES} \leq 230$ cm
average CES χ^2	≤ 20
Had/Em	$\leq 0.055 + 0.00045 \times E$
corrected CalIso0.4	$\leq 0.1 \times E_T$ if $E_T < 20$ GeV or $\leq 2.0 + 0.02 \times (E_T - 20)$
TrkIso0.4	$\leq 2.0 + 0.005 \times E_T$
$N3D$ tracks in cluster	≤ 1
track P_T if $N3D = 0$	$\leq 1.0 + 0.005 \times E_T$
E_T of 2 nd CES cluster (wire and strip)	$\leq 0.14 \times E_T$ if $E_T < 18$ GeV $\leq 2.4 + 0.01 \times E_T$ if $E_T \geq 18$ GeV
Additional Photon ID Cuts	
PMT Asymmetry	$A = pmt1 - pmt2 / (pmt1 + pmt2) < 0.65$
Phoenix	Reject Photons Matched to Phoenix Track

Table 4: Summary of the photon ID and isolation cuts. These are the standard cuts with the addition of PMT asymmetry and Phoenix rejection cuts.

with a more energetic semi-hard interaction (often referred to as a Min-Bias interaction) giving the highest $\sum P_T$ vertex. A wrong vertex choice results in mis-measured E_T of both photon candidates, thus it causes fake \cancel{E}_T . Although this mis-measurement is small in most cases, sometimes it can give a very large value of fake \cancel{E}_T if the two vertices are far apart or if the original photons are very energetic. Fortunately, this effect can be easily corrected by a vertex re-assignment. For every event with multiple class 12 vertices we recalculate the photon E_T with respect to every vertex of class 12 with $|Z_{vx}| \leq 60$ cm and select the one that gives the smallest \cancel{E}_T . The standard vertex requirements with vertex re-assignment are listed in Table 5. As a result of this procedure some photons fall below the $E_T^\gamma \geq 13$ GeV threshold and are removed from the final sample. Events that start with $E_T^\gamma < 13$ GeV are not added back. This procedure is followed for background and signal estimation.

Vertex Requirements
At least one vertex of class 12 with $ Z_{vx} \leq 60$ cm
The highest $\sum P_T$ vertex as a primary vertex
For events with multiple vertices Recalculate the photon E_T for every vertex with $ Z_{vx} \leq 60$ cm and pick the one that gives smallest \cancel{E}_T

Table 5: Summary of the vertex requirements and vertex re-assignment algorithms.

Additional requirements are placed on the sample to reduce non-collision backgrounds. Muons from beam halo are known to fake the photon signature [31, 32]. Because such events are not related to a hard interaction and usually appear only in one calorimeter wedge, they also create large \cancel{E}_T . To suppress contribution due to this background, we first loop over all photons in an event to identify beam halo candidates using the beam halo ID cuts in Table 6 [32]. Then we reject the

event if it has two beam halo candidates separated by $|\Delta\phi| < 30^\circ$ (within neighboring wedges). Events with a single beam halo candidate overlap with a SM $\gamma + jet$ event have been shown to be negligible and we have ignored them here [21].

A photon is identified as being from a B.H. muon if	
Cuts	values
seedWedge	>9
NHadPlug	>2
seedWedgeHadE	$< [0.4 + (0.019(N_{vx12} - 1) + 0.013)seedWedge] \text{ GeV}$
wedge number	0 or 23

Table 6: Summary of requirements to identify photons from beam halo sources. For more detail see Ref. [32]. Events are rejected if they are two beam halo candidates which are separated by $|\Delta\phi| < 30^\circ$.

A cosmic ray muon that traverses the detector can also help fake the $\gamma\gamma + \cancel{E}_T$ signature. These events can be rejected based on our ability to identify them from the fact that they are not correlated in time with collisions, and therefore their arrival time distribution is roughly flat. The difference in arrival time of the first and second photons from cosmic rays is also proportional to the spatial separation between these two photons; photons from real $\gamma\gamma$ events arrive almost coincidentally in time. Thus, to suppress contributions from cosmic ray sources, we use the EMTiming system [20] to apply timing cuts to reduce the contamination due to cosmic rays [31, 32]. We reject an event if either photon is more than 4σ from being consistent with coming from the interaction or if the two photons are well separated in time indicating they are from a cosmic. The cosmic ray rejection cuts are listed in Table 7.

An event is identified as a cosmic ray if
Either $ T_{\gamma 1} \text{ or } T_{\gamma 2} > 4\sigma_T$, where $\sigma_T = 1.665 \text{ ns}$ or $ \Delta T_{\gamma\gamma} = T_{\gamma 1} - T_{\gamma 2} > 4\sigma_{\Delta T}$, where $\sigma_{\Delta T} = 1.021 \text{ ns}$

Table 7: Summary of the EMTiming cuts to remove cosmic ray events. T is the EMTiming recorded value with only slewing corrections [20].

The last set of global cuts we apply are the \cancel{E}_T cleanup cuts. We remove events where \cancel{E}_T is likely to be due to a severe energy mis-measurement of a photon or jet. Such cases include the so-called *Tower-9* effect [33], energy lost in ϕ -cracks between CEM towers, or when a photon (or π^0) is lost in the central or forward crack leaving only a signature of a small jet. Therefore, we reject an event if the second photon or any jet is pointing right at the \cancel{E}_T . The full set of \cancel{E}_T cleanup cuts are listed in Table 8.

After all cuts our preselection sample consists of 38,053 events left after all the quality, ID and cleanup cuts are applied. Table 9 gives a summary of the event reduction.

Case	The event is removed if
For 2nd photon with $\Delta\phi(\cancel{E}_T - \gamma 2) < 0.3$	$ \eta_{det}(\gamma 2) > 1.0$ or $ \eta_{det}(\gamma 2) < 0.1$ or $ X_{CES}(\gamma 2) > 18.5$ cm
For any jet ($ \eta_{det}(jet) < 2.5$, $E_T > 5$ GeV, $N_{twr} < 10$, $N_{trk} < 5$ with $\Delta\phi(\cancel{E}_T - jet) < 0.3$	$EmFr > 0.875$ and $ \eta_{det}(jet) < 1.1$ or $EmFr < 0.3$ and $(\eta_{det}(jet) < 0.1$ or $ \eta_{det}(jet) - 1.15 < 0.05$)

Table 8: Summary of the \cancel{E}_T cleanup cuts. Note N_{twr} is the number of calorimeter towers in the jet and N_{trk} is the number of tracks associated with the jet.

Requirements	Signal sample (events passed)
Trigger, Goodrun, and Standard photon ID with $ \eta < 1.1$ and $E_T > 13$ GeV	45,275
Phoenix rejection	41,418
PMT spike rejection	41,412
Vertex requirements	41,402
$E_T^{swap} > 13$ GeV after vertex swap	39,719
Beam Halo rejection	39,713
Cosmic rejection (EMTiming cut)	39,663
\cancel{E}_T cleanup cuts	38,053

Table 9: Summary of the $\gamma\gamma + \cancel{E}_T$ presample selection requirements and the event sample reduction. The trigger requirements are given in Table 3, the photon ID and isolation, Phoenix and PMT requirements are described in Table 4, the vertex requirements and vertex swap are described in Table 5, the beam halo rejection requirements are described in Table 6, the cosmic rejection requirements are given in Table 7 and the \cancel{E}_T cleanup cuts are given in Table 8.

3 Backgrounds

3.1 Overview

The final signal region for this analysis is defined by the subsample of preselection events that also pass a set of optimized final kinematic cuts. The methods for determining the number of expected background events in the signal region are based on a combination of data and MC and allow for a large variety of potential final sets of cuts. We use these estimates as part of the optimization procedure described in Section 6. In this section we describe the backgrounds and the methods used to estimate the background rates and their uncertainties.

There are three major sources of background for \cancel{E}_T in $\gamma\gamma$ events:

- QCD events with fake \cancel{E}_T :
 - a) true $\gamma\gamma$, γ -jet $\rightarrow \gamma\gamma_{fake}$, and jet-jet $\rightarrow \gamma_{fake}\gamma_{fake}$ events where \cancel{E}_T arises due to standard energy resolution mis-measurements in the calorimeter; b) large fake \cancel{E}_T due to pathologies such as wrong vertex events where one or both photon candidates are coming from a vertex other than the highest $\sum P_T$ primary vertex, causing a systematic mis-measurement of the \cancel{E}_T or tri-photon events with a lost photon that creates the fake \cancel{E}_T .
- Electroweak events with real \cancel{E}_T :
 - a) charged leptonic channels: i) from $W\gamma\gamma$ and $Z\gamma\gamma$ events where both photons are real; ii) from $W\gamma$ and $Z\gamma$ events with a fake photon; iii) from W and Z events where both photon candidates are fake photons; iv) $t\bar{t}$ production and decay.
 - b) neutral leptonic channels: $Z\gamma\gamma \rightarrow \nu\bar{\nu}\gamma\gamma$, $Z\gamma \rightarrow \nu\bar{\nu}\gamma + \gamma_{fake}$ or $Z \rightarrow \nu\bar{\nu} + \gamma_{fake}\gamma_{fake}$.
- Non-collision events:
 - a) PMT spikes; b) cosmic ray; c) beam-halo events where one or more of the photons and \cancel{E}_T are not related to the collision.

We next discuss each in detail, how it is estimated and how the uncertainties are calculated.

3.2 QCD Backgrounds with Fake \cancel{E}_T

Here we describe the QCD backgrounds and our techniques used to predict the number of expected events in the signal region after all kinematic requirements. These backgrounds come in two different categories; fake \cancel{E}_T due to gaussian energy mis-measurements in the calorimeter as measured by our *Met Model* ($N_{\text{signal}}^{\text{MetModel}}$) and fake \cancel{E}_T from pathologies ($N_{\text{signal}}^{\text{PATH}}$) such as picking the wrong vertex in events where true collision did not create a vertex with no vertex or tri-photon events with a lost photon. The total QCD background prediction in the signal region, $N_{\text{signal}}^{\text{QCD}}$ is given by

$$N_{\text{signal}}^{\text{QCD}} = N_{\text{signal}}^{\text{MetModel}} + N_{\text{signal}}^{\text{PATH}} \quad (2)$$

3.2.1 QCD Background due to Energy Mismeasurements in the Calorimeter

Standard Model QCD events, $\gamma\gamma$, γ -jet $\rightarrow \gamma\gamma_{fake}$, and jet-jet $\rightarrow \gamma_{fake}\gamma_{fake}$, are the dominant sources of events in the diphoton presample and a major background for $\gamma\gamma + \cancel{E}_T$. The energy fluctuations in the calorimeter, which lead to considerable values of fake \cancel{E}_T , happen only in a small fraction of cases, but huge cross sections for these processes make them one of the largest

backgrounds. However, rather than measure \cancel{E}_T , we can significantly reduce the QCD background by selecting events based on \cancel{E}_T *Significance*, using a new *Met Resolution Model* [21].

The *Met Resolution Model* considers the clustered and unclustered energy in the event and calculates a probability, $P(\cancel{E}_T^{fluct} > \cancel{E}_T)$, for fluctuations in the energy measurement to produce \cancel{E}_T^{fluct} equivalent to or larger than the measured \cancel{E}_T . This probability is then used to define a \cancel{E}_T *Significance* as $-\log_{10}(P_{\cancel{E}_T^{fluct} > \cancel{E}_T})$. Events with true and fake \cancel{E}_T of the same value should have, on average, different \cancel{E}_T *Significance*. By construction a \cancel{E}_T *Significance* cut of 3, 4, and 5 allows $\sim 0.1\%$, $\sim 0.01\%$, and $\sim 0.001\%$ of QCD events respectively. Thus if we suppose our data sample has N_{events} events, which have no intrinsic \cancel{E}_T in any events coming from energy mis-measurements only, then the *true* (perfect) \cancel{E}_T *Significance* has a simple *a priori* distribution given by

$$\frac{dN}{dx} = N_{\text{event}} \cdot \ln(10) \cdot 10^{-x} \quad (3)$$

where $x = \cancel{E}_T$ *Significance*. We will use this equation to calculate the estimated rate of Gaussian fluctuation passing the final kinematic cuts in Section 3.2.2.

This model assumes only two sources of mis-measurements that cause fake \cancel{E}_T . Mismeasurements from 1) jet energy clusters (jets) and 2) soft, unclustered energy (underlying event or multiple interactions). Individual contributions of each of these components to \cancel{E}_T are modeled according to their energy resolution functions [21]. Jets are collimated sprays of energetic particles in a certain direction and can cause significant \cancel{E}_T . The unclustered energy tends to be small and uniformly spread in the calorimeter, making the portion of \cancel{E}_T due to this source is usually small.

We predict $N_{\text{signal}}^{\text{MetModel}}$, the QCD contribution of the background with fake \cancel{E}_T that passes the kinematic cuts using the *Met Model*. To estimate the expected \cancel{E}_T *Significance* for a data sample (the number of events above a given \cancel{E}_T *Significance* cut after kinematic cuts), we consider the jets and unclustered energy in each event passing the other kinematic cuts. For each data event we throw 10 pseudo-experiments to generate a \cancel{E}_T and calculate its significance, according to the jets and underlying event configuration. Then we count the number of pseudo-experiments that pass our \cancel{E}_T *Significance* cuts. This number divided by the number of pseudo-experiments gives us a prediction for the QCD background due to energy mis-measurements for the number of events in a data sample passing the kinematic cuts. In this way for any set of kinematic cuts we can predict the \cancel{E}_T *Significance* and other kinematic distributions. After estimating this background, the expected \cancel{E}_T and \cancel{E}_T *Significance* distributions of QCD are shown in Figure 4 for the presample. For completeness we include the H_T and $\Delta\phi(\gamma_1, \gamma_2)$ distributions.

The systematic uncertainty on the number of events above a \cancel{E}_T *Significance* cut is evaluated by comparing the *Met Model* predictions with the default set of model parameters to predictions obtained with the parameters deviated by $\pm\sigma$. The total uncertainty is estimated by adding the statistical uncertainty and these systematic uncertainties in quadrature.

3.2.2 Fake \cancel{E}_T from QCD with Events Reconstruction Pathologies

A source of QCD background that is unaccounted for by the *Met Model* is diphoton events with a wrong choice of the primary interaction vertex. This occurs when a $\gamma\gamma$ pair is produced by one interaction and, for example, a pair of jets is produced at another vertex and produces the highest $\sum P_T$ vertex. Hard scattering processes involving jets have, in general, more tracks compared to interactions where no jets are produced. Therefore, if one vertex produces jets and the other one produces only a $\gamma\gamma$ pair, then it is very likely that the former vertex will be picked as a primary

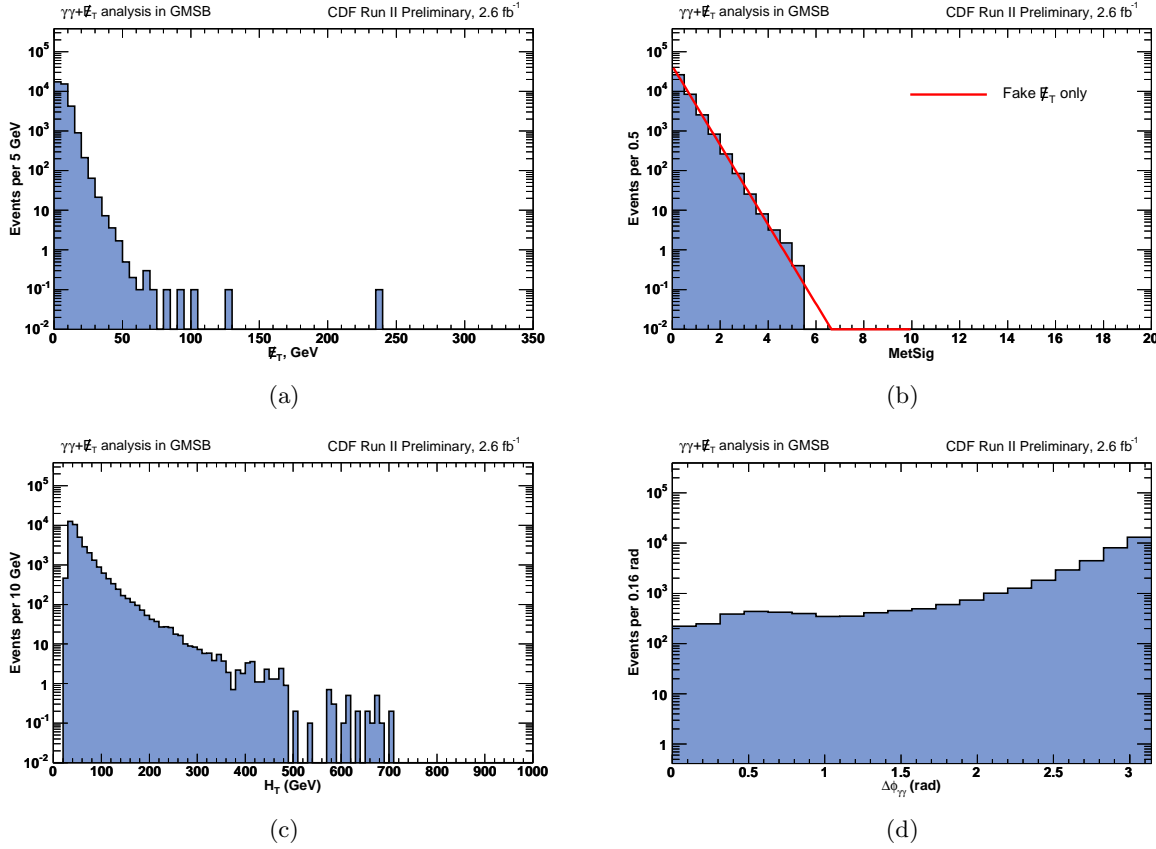


Figure 4: The QCD background predictions using the *Met Model* for the presample. (a), (b), (c) and (d) show \cancel{E}_T , \cancel{E}_T *Significance*, H_T and $\Delta\phi(\gamma_1, \gamma_2)$ distributions respectively. The red solid line in (b) shows the perfect prediction of fake \cancel{E}_T from energy mismeasurements only having no intrinsic \cancel{E}_T . In this case, the perfect prediction of \cancel{E}_T *Significance* has a simple *a priori* distribution of $dN/dx = N_{\text{event}} \times \ln(10) \times 10^{-x}$. Note that \cancel{E}_T and \cancel{E}_T *Significance* are from the *Met Model*. However the H_T and $\Delta\phi(\gamma_1, \gamma_2)$ are just the distributions from the presample which is dominated by QCD with small \cancel{E}_T *Significance* as shown in (b).

one. The wrong vertex results in \cancel{E}_T mis-measurement and can give fake \cancel{E}_T . As described in Section 2.2, this effect can usually be corrected by the vertex re-assignment procedure. However, there are situations when the vertex swap procedure cannot fix large fake \cancel{E}_T . This happens when the $\gamma\gamma$ interaction does not produce a reconstructed vertex at all, for example with large $|Z_{vx}|$. The *Met Model* will not be able to account for this background since this effect is not Gaussian in nature, and the unclustered energy parameterization does not include it.

A third class of QCD events, whose contribution to the $\gamma\gamma + \cancel{E}_T$ signature is not estimated by the *Met Model*, are tri-photon events with a lost photon². The cross section of this process is very small. However, the probability to lose a photon in the calorimeter cracks is on the order of $\sim 10\%$ or more³, so that the probability to lose one of the photon candidates in a tri-photon event can be $\sim 30\%$ or larger.

To obtain the prediction for all events reconstruction pathologies in the QCD background at the same time, we model it using a PYTHIA $\gamma\gamma$ sample, “cdfpstn:gx0s1g”, with large statistics, and subtract off the expectations for Gaussian fluctuations in the MC and normalize to data. The final prediction of these QCD backgrounds is given by

$$N_{\text{signal}}^{\text{PATH}} = (N_{\text{signal}}^{\text{PATH-MC}} - N_{\text{signal}}^{\text{MM-MC}}) \cdot \text{SF}_{\text{QCD}} \quad (4)$$

where $N_{\text{signal}}^{\text{MM-MC}}$ is the estimated rate of Gaussian fluctuation passing the final kinematic cuts, and SF_{QCD} is a scale factor to normalize the MC sample to the data and take into account the fact that the MC has only $\gamma\gamma$ events, whereas QCD backgrounds come from $\gamma\gamma$, $\gamma - \text{jet}$, or $\text{jet} - \text{jet}$ sources. The estimated rate of Gaussian fluctuation passing the final cuts is given by

$$N_{\text{signal}}^{\text{MM-MC}} = N_{\text{signal}}^{\text{noMetSig cut}} \cdot R_{\text{MetSig}}^{\text{exp}} \quad (5)$$

where $N_{\text{signal}}^{\text{noMetSig cut}}$ is the number of events that pass all kinematic cuts but \cancel{E}_T *Significance* cut in the $\gamma\gamma$ MC and $R_{\text{MetSig}}^{\text{exp}}$ is the expected rate for \cancel{E}_T *Significance* cut using Eq.(2). The scale factor is taken to be equal to the number of events passing the preselection cuts in data and in the MC sample. The number of events that pass the preselection cuts for data ($N_{\text{presample}}^{\text{QCD-Data}}$) and MC ($N_{\text{presample}}^{\text{QCD-MC}}$) are 38,053 and 283,554 respectively. We find

$$\text{SF}_{\text{QCD}} = \frac{N_{\text{presample}}^{\text{QCD-Data}}}{N_{\text{presample}}^{\text{QCD-MC}}} = \frac{38,053}{283,554} = 0.134 \pm 0.007 \quad (\text{stat.only}). \quad (6)$$

The expected \cancel{E}_T , \cancel{E}_T *Significance*, H_T and $\Delta\phi(\gamma_1, \gamma_2)$ distributions for the $\gamma\gamma$ MC sample passing the preselection cuts are shown in Figure 5.

The systematic uncertainties on this background prediction include the uncertainty on the scale factor and the uncertainty due to MC-data differences in the unclustered energy parameterization and the jet energy scale. To get the systematic uncertainty on the unclustered energy parametrization from the *Met Model* we deviate the default set of parameters by $\pm\sigma$. For the systematic uncertainty on the jet energy scale we follow the standard procedure at CDF [34]. The total uncertainty is estimated by adding the statistical uncertainty and these systematic uncertainties in quadrature.

²One of the photon candidates can be a fake.

³This is an educated guess, and it is based on a fact that the CEM ϕ -cracks alone account for $\sim 8\%$ of the CEM area. This number is not used in the analysis, rather it is just given as a value which indicates to the reader the magnitude to indicate that this is an important background.

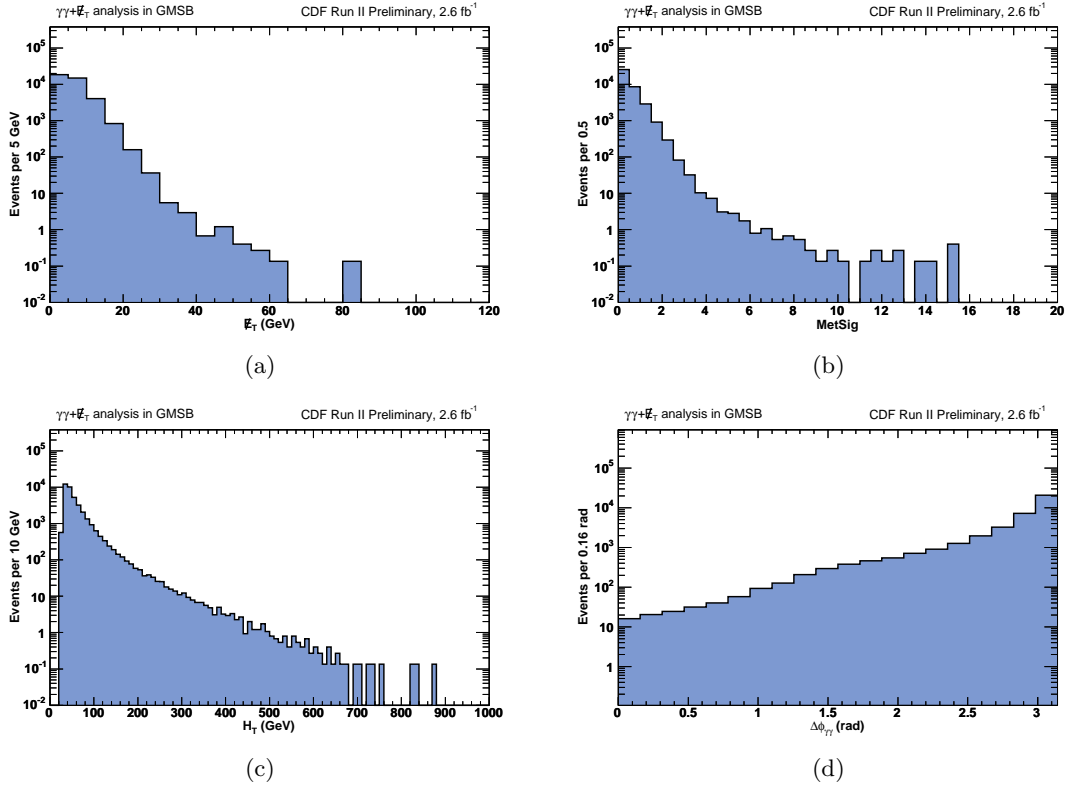


Figure 5: The QCD background from the all pathologies in the 286,391 PYTHIA $\gamma\gamma$ MC sample after the preselection requirements, but normalized by the SF_{QCD} scale factor. (a), (b), (c), and (d) show the E_T , E_T Significance, H_T , and $\Delta\phi(\gamma_1, \gamma_2)$ distributions respectively. The tails in E_T Significance are long, but the overall rate of this process is low.

We describe QCD backgrounds from wrong vertex and tri-photon events separately to cross check our estimations from event reconstruction pathologies in Appendix III.

3.3 Electroweak Backgrounds with Real \cancel{E}_T

Electroweak processes involving W 's and Z 's are the most common source of real \cancel{E}_T in $p\bar{p}$ collisions. We estimate both charged leptonic decays and neutral leptonic decays.

3.3.1 Charged Leptonic Decay Channels

There are four ways we can get a $\gamma\gamma + \cancel{E}_T$ signature in charged leptonic electroweak events: 1) from $W\gamma\gamma$ and $Z\gamma\gamma$ events where both photons are real; 2) from $W\gamma$ and $Z\gamma$ events with a fake photon; 3) from W and Z events where both photon candidates are fake photons; 4) $t\bar{t}$ production and decay. As we will see, out of these sources, $Z\gamma \rightarrow \mu\mu\gamma$ events are the dominant electroweak background in our analysis after all kinematic requirements.

To estimate the contribution from the electroweak backgrounds we use the standard electroweak MC samples [35], according to their production cross section and k-factors, but normalized to data. The Baur $W\gamma$ and $Z\gamma$ stntuples are used to evaluate contributions from both $W/Z + \gamma$ and $W/Z + \gamma\gamma$ events from ISR/FSR. The inclusive PYTHIA W and Z stntuples are used to obtain a contribution from $W + \text{jet}$, $Z \rightarrow e^+e^-/\tau^+\tau^-$, and $Z + \text{jet}$ events where both photon candidates are fakes and $t\bar{t}$ events. We consider all three leptonic decay modes of W and Z bosons. To avoid overlaps between Baur and PYTHIA, we filter out PYTHIA events where photons reconstructed in the detector are matched to HEPG level photons from either quark ISR or lepton FSR.

The electroweak background predictions are given by

$$N_{\text{signal}}^{\text{EWK}} = \sum_{i=0}^n N_{\text{signal},i}^{\text{EWK-MC}} \cdot \text{SF}_i \cdot \left(\frac{N_{e\gamma,\text{signal}}^{\text{Data}}}{N_{e\gamma,\text{signal}}^{\text{MC}}} \right) \quad (7)$$

where $N_{\text{signal},i}^{\text{EWK-MC}}$ is the number of events passing all the final kinematic cuts from MC sample i , each electroweak source. The scale factors, SF_i normalizes each electroweak background to its production cross section and k-factor. To minimize the dependence of our predictions on potential Data-MC differences (trigger efficiencies, acceptance and ID efficiencies, k-factors, modeling of ISR/FSR, PDF uncertainties, luminosity uncertainties, etc.), we normalize the MC's to a sample of $e\gamma$ events that also pass all signal kinematic cuts $\left(\frac{N_{e\gamma,\text{signal}}^{\text{Data}}}{N_{e\gamma,\text{signal}}^{\text{MC}}} \right)$. To minimize differences between $e\gamma$ and $\gamma\gamma$ samples, electrons are required to satisfy the photon-like ID requirements listed in Table 10. Here and later we will refer to the ratio of $\left(\frac{N_{e\gamma,\text{signal}}^{\text{Data}}}{N_{e\gamma,\text{signal}}^{\text{MC}}} \right)$ to be the global electroweak normalization factor.

The scale factors are calculated using

$$\text{SF}_i = \frac{\sigma_i \cdot k_i \cdot \mathcal{L}}{N_{\text{sample},i}^{\text{EWK}}} \quad (8)$$

where σ_i is production cross section, k_i is the k-factor, \mathcal{L} is the 2.6 fb^{-1} of luminosity and $N_{\text{sample},i}^{\text{EWK}}$ is the number of events in the MC sample after passing goodrun. The results are summarized in Table 11. The normalization to data term, $N_{e\gamma,\text{signal}}^{\text{MC}}$, is calculated using

The Standard Photon-like Electron ID Cuts	
detector	CEM
Conversion*	No
corrected E_T	≥ 13 GeV
CES fiduciality	$ X_{\text{CES}} \leq 21$ cm $9 \text{ cm} \leq Z_{\text{CES}} \leq 230$ cm
average CES χ^2	≤ 20
Had/Em	$\leq 0.055 + 0.00045 \times E$
corrected CalIso0.4	$\leq 0.1 \times E_T$ if $E_T < 20$ GeV or $\leq 2.0 + 0.02 \times (E_T - 20)$
$N3D$ tracks in cluster*	1 or 2
E/P of 1 st track*	$0.8 \leq E/P \leq 1.2$ if $P_T < 50$ GeV no cut if $P_T \geq 50$ GeV
2 nd track P_T if $N3D = 2^*$	$\leq 1.0 + 0.005 \times E_T$
$TrkIso0.4 - P_T^{1^{st}trk}$	$\leq 2.0 + 0.005 \times E_T$
E_T of 2 nd CES cluster (wire and strip)	$\leq 0.14 \times E_T$ if $E_T < 18$ GeV $\leq 2.4 + 0.01 \times E_T$ if $E_T \geq 18$ GeV
$\Delta z = z_{trk} - z_{vx}^*$	$ \Delta z \leq 3$ cm

Table 10: Photon-like electron ID cuts used to make the $e\gamma$ data set. Cuts that are different from the standard photon ID and isolation, given in Table 4, are indicated with a *. Also, no additional cuts in Table 4 such as PMT spikes and Phoenix rejection cuts are added.

$$N_{e\gamma, \text{signal}}^{\text{MC}} = \sum_{i=0}^n N_{e\gamma, \text{signal}, i}^{\text{MC}} \cdot \text{SF}_i. \quad (9)$$

The uncertainty on the electroweak backgrounds are dominated by the $e\gamma$ normalization factor uncertainty. This includes data and MC statistical uncertainties and differences in MC modeling. The last uncertainty is estimated by comparing results for a default value of the E/p cut ($0.8 < E/p < 1.2$) and a deviated value of the E/p cut ($E/p < 2.0$) for variation of scale factor as a function of the cuts. This will be compared to the overall scale factor as the final kinematic requirements are varied. The total uncertainties include the MC statistical uncertainties and uncertainties on the normalization factors added in quadrature.

3.3.2 Neutral Leptonic Decay Channels

To indirectly estimate electroweak backgrounds from neutral leptonic channels such as $Z\gamma\gamma \rightarrow \nu\bar{\nu}\gamma\gamma$, $Z\gamma \rightarrow \nu\bar{\nu}\gamma + \gamma_{fake}$ or $Z \rightarrow \nu\bar{\nu} + \gamma_{fake}\gamma_{fake}$, we use MadGraph $Z(\mu^+\mu^-) + \gamma\gamma$ sample at this moment. Using this sample we remove photons from lepton FSR to estimate $Z\gamma\gamma \rightarrow \nu\bar{\nu}\gamma\gamma$ since neutrinos do not radiate photons. To select the $\gamma\gamma$ events we look at Z mass window, $86 < M_Z < 96$ GeV, at HEPG level and count the number of events therein. We have 0.11 ± 0.03 events from this background after optimal cuts described in Section 6 and use it temporally.

The expected \mathbb{E}_T , \mathbb{E}_T Significance, H_T and $\Delta\phi(\gamma_1, \gamma_2)$ distributions for electroweak background in the presample is shown in Figure 6.

Background Source	Cross Section $\sigma_i(\text{pb})$	k-factor k_i	MC events $N_{\text{EWK sample},i}$	MC-to-Data SF SF_i
$W(e) + \gamma$	32.0	1.36	1,775,122	0.0635
$W(\mu) + \gamma$	32.0	1.34	1,836,273	0.0605
$W(\tau) + \gamma$	32.0	1.34	1,824,182	0.0609
$Z(e) + \gamma$	10.3	1.36	9,258,132	0.0039
$Z(\mu) + \gamma$	10.3	1.36	9,214,135	0.0040
$Z(\tau) + \gamma$	10.3	1.36	9,196,501	0.0040
$W(e) + \gamma$ no ISR/FSR	1,960	1.4	33,815,147	0.210
$W(\mu) + \gamma$ no ISR/FSR	1,960	1.4	23,058,663 (10,166,426)	0.308 (0.699)
$W(\tau) + \gamma$ no ISR/FSR	1,960	1.4	24,057,340	0.296
$Z(e) + \gamma$ no ISR/FSR	355	1.4	22,986,333	0.056
$Z(\mu) + \gamma$ no ISR/FSR	355	1.4	14,704,660 (10,203,233)	0.0876 (0.126)
$Z(\tau) + \gamma$ no ISR/FSR	355	1.4	33,278,066	0.0387
$t\bar{t}$ (incl.)	6.7	N/A	7,430,826	0.0023

Table 11: Scale factors for the individual electroweak backgrounds. Note that the scales factors for $W(\mu) + \gamma$ no ISR/FSR and $Z(\mu) + \gamma$ no ISR/FSR are listed twice. For these two samples only parts of the samples were used in the $e\gamma$ counting experiment as they are low rate processes.

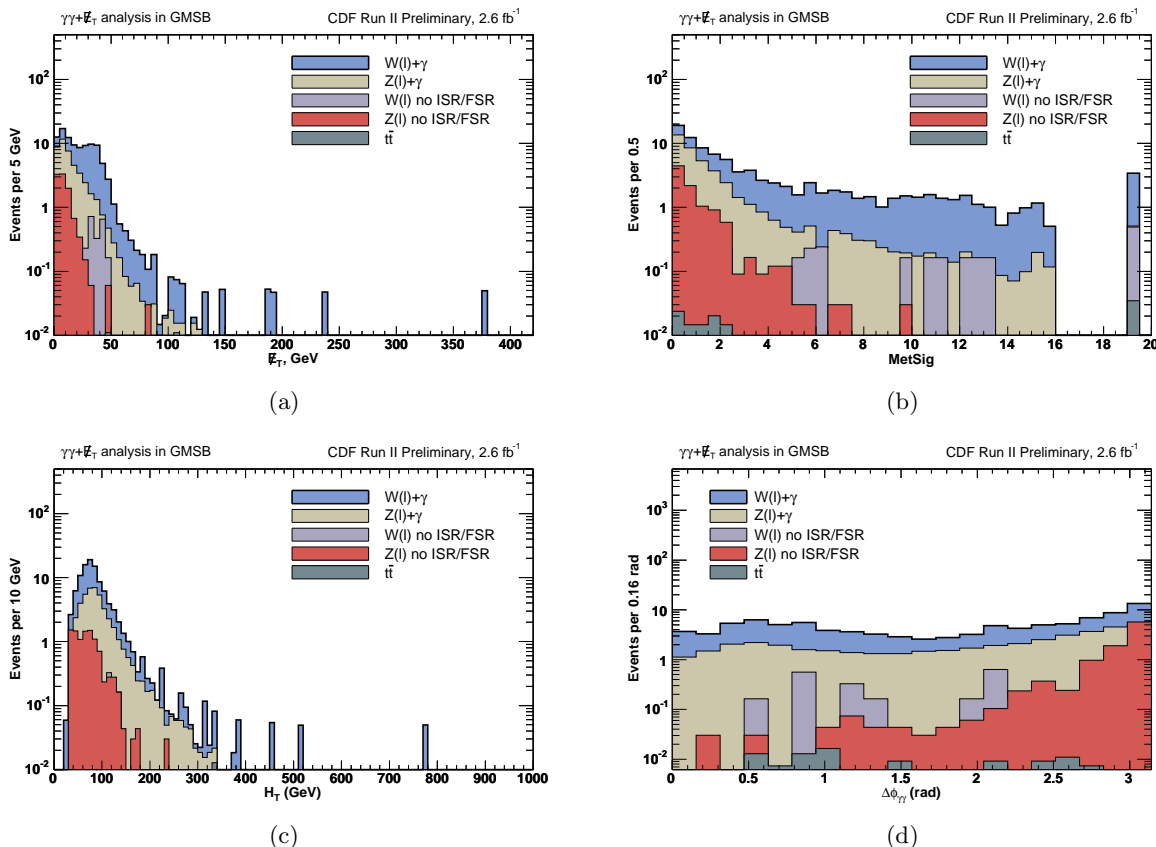


Figure 6: The electroweak background predictions after the preselection requirements. (a), (b), (c), and (d) show the \cancel{E}_T , \cancel{E}_T Significance, H_T , and $\Delta\phi(\gamma_1, \gamma_2)$ distributions respectively. The global scale factor for the preselection cuts, 0.78, is used.

3.4 Non-Collision Events

Non-Collision backgrounds to the $\gamma\gamma + \cancel{E}_T$ background come from PMT spikes, beam halo (B.H.) and cosmic rays (C.R.) where either a single or double photon-like signature comes from the non-collision source. Because these events do not originate from beam-beam interactions, they can be a source of significant spurious \cancel{E}_T . It was shown in [25] that other sources of spurious energy in $\gamma\gamma$ events are negligible.

PMT spikes are rare and have a distinct signature (see Ref. [31]). The PMT asymmetry removes them very efficiently. Therefore, we do not explicitly evaluate this background and take the number of remaining PMT spikes backgrounds events to be zero. We next discuss beam halo and cosmic rays.

3.4.1 Beam Halo Events

As discussed in Ref. [31] B.H. events fake the $\gamma\gamma + \cancel{E}_T$ final state when high energy muons, produced in beam-beam pipe interactions, interact with the calorimeter and fake two photons. For geometric reasons these photon candidates are mostly located in the same wedge, mostly wedges 0 and 23 after. Since as previously mentioned, single γ B.H. overlapping a γ event is negligible [21].

To estimate the B.H. contribution to the $\gamma\gamma + \cancel{E}_T$ final state after the B.H. rejection procedure described in Section 2.2, we use a loose beam halo enriched $\gamma\gamma$ sample. These events are used to predict the shape of the kinematic distributions and their correlations. We then correct for differences between the loose cut samples requirements, to predict the expected number of BH events after all final cuts. The B.H. enriched sample is selected as having two loose photon candidates passing the requirements of Table 12, and identified as a beam halo (Table 6). To increase the statistics we do not require a vertex, nor do we reject events that fail the EMTiming requirements. We will correct for this also. A total of 13 events, $N_{\text{control}}^{\text{BH}}$, make up this sample. We use all 13 events as a template for the \cancel{E}_T and other kinematic distributions, shown in Figure 7

To take this sample to the prediction of the number of events in the signal region we multiply by the measured rate at which these events pass the kinematic cuts as well as the rate they pass the ID and isolation, vertex and timing cuts. Finally we take into account the efficiency for B.H. events to be in this sample. The B.H. ID requirements are 90% efficient in identifying B.H. events, so we take $R_{\text{BH}} = 0.9 = 90\%$ as the rejection power, taken from Ref. [21]. Using these pieces we calculate as follows:

$$N_{\text{signal}}^{\text{BH}} = N_{\text{control}}^{\text{BH}} \cdot R_{\text{ID}, \text{VX}, \text{T}}^{\text{BH}} \cdot R_{\text{kinematic}}^{\text{BH}} \cdot \frac{1}{\epsilon_{\text{BH}}} \quad (10)$$

where $R_{\text{ID}, \text{VX}, \text{T}}^{\text{BH}}$ is the rejection factor that takes into account the rejection power of the not applied on the control sample for the photon ID and isolation, vertex and timing cuts, $R_{\text{kinematic}}^{\text{BH}}$ estimates the rejection factor for the kinematic requirements and $\frac{1}{\epsilon_{\text{BH}}}$ takes into account the fraction of B.H. events that are not in our sample. The first rejection factor, $R_{\text{ID}, \text{VX}, \text{T}}^{\text{BH}}$, is estimated by

$$R_{\text{ID}, \text{VX}, \text{T}}^{\text{BH}} = \frac{N_{\text{ID}, \text{VX}, \text{T}}^{\text{BH-control}}}{N_{\text{control}}^{\text{BH}}} = \frac{1}{13} \quad (11)$$

where $N_{\text{ID}, \text{VX}, \text{T}}^{\text{BH-control}} = 1$ is the number of events in the control sample that also pass the photo ID and isolation requirements, vertex requirements and the EMTiming cuts. The $R_{\text{kinematic}}^{\text{BH}}$, rejection factor for the final kinematic cuts is estimated by

$$R_{\text{kinematic}}^{\text{BH}} = \frac{N_{\text{kinematic}}^{\text{BH-control}}}{N_{\text{control}}^{\text{BH}}} = \frac{N_{\text{kinematic}}^{\text{BH-control}}}{13} \quad (12)$$

where $N_{\text{kinematic}}^{\text{BH-control}}$ is the number of events in the control sample that also pass the final kinematic cuts described in Section 6. To normalize to the lost rate of B.H. events in our sample we take

$$\frac{1}{\epsilon_{\text{BH}}} = \frac{(1 - R_{\text{BH}})}{R_{\text{BH}}} = \frac{1 - 0.9}{0.9} = 0.111 \quad (13)$$

Thus, the final expected number of B.H. events in the signal region that pass the final kinematic cuts described in Section 6 using the scale factor is given by

$$\begin{aligned} N_{\text{signal}}^{\text{BH}} &= N_{\text{control}}^{\text{BH}} \cdot R_{\text{ID,VX,T}}^{\text{BH}} \cdot R_{\text{kinematic}}^{\text{BH}} \cdot \frac{1}{\epsilon_{\text{BH}}} \\ &= 13 \cdot \frac{1}{13} \cdot \frac{N_{\text{kinematic}}^{\text{BH-control}}}{13} \cdot 0.111 \\ &= N_{\text{kinematic}}^{\text{BH-control}} \cdot (0.008) \\ &= N_{\text{kinematic}}^{\text{BH-control}} \cdot \text{SF}_{\text{BH}} \end{aligned} \quad (14)$$

where we take $\text{SF}_{\text{BH}} = 0.008 \pm 0.008$ (stat. only).

The uncertainties on B.H. estimation are dominated by the statistical uncertainty on the number of events after all kinematic cuts in the B.H. control sample, $N_{\text{kinematic}}^{\text{BH-control}}$. The other source of uncertainty, though much smaller, is the uncertainty on fraction of B.H. events that pass the EMTiming cuts.

Cuts	Loose control sample ID
detector	CEM
corrected E_T	$\geq 13 \text{ GeV}$
CES fiduciality	$ X_{\text{CES}} \leq 21 \text{ cm}$ $9 \text{ cm} \leq Z_{\text{CES}} \leq 230 \text{ cm}$
average CES χ^2	≤ 20
Had/Em*	≤ 0.125
corrected CallIso0.4*	$\leq 0.15 \times E_T$ if $E_T < 20 \text{ GeV}$ or $\leq 3.0 + 0.02 \times (E_T - 20)$
TrkIso0.4	≤ 5
$N3D$ tracks in cluster*	≤ 1
track P_T if $N3D = 0$ *	$\leq 0.25 \times E_T$
E_T of 2 nd CES* cluster (wire and strip)	no cut

Table 12: Summary of the standard loose photon ID cuts used to create our non-collision enriched background samples. Cuts that are different from the standard photon ID and isolation requirements without the two additional requirements, PMT and Phoenix cuts, given in Table 4, are indicated with a *.

DIPHOTON_12, DIPHOTON_18, PHO_50 or PHO_70 trigger
Two photons passing the loose photon ID cuts in Table 12
No vertex requirements
$ T_{\gamma_1} $ or $ T_{\gamma_2} < 20$ ns
Two photons identified by Beam Halo ID cuts listed in Table 6
$\cancel{E}_T > 20$ GeV

Table 13: Summary of cuts to select the beam halo enriched sample. A total of 13 events pass these requirements.

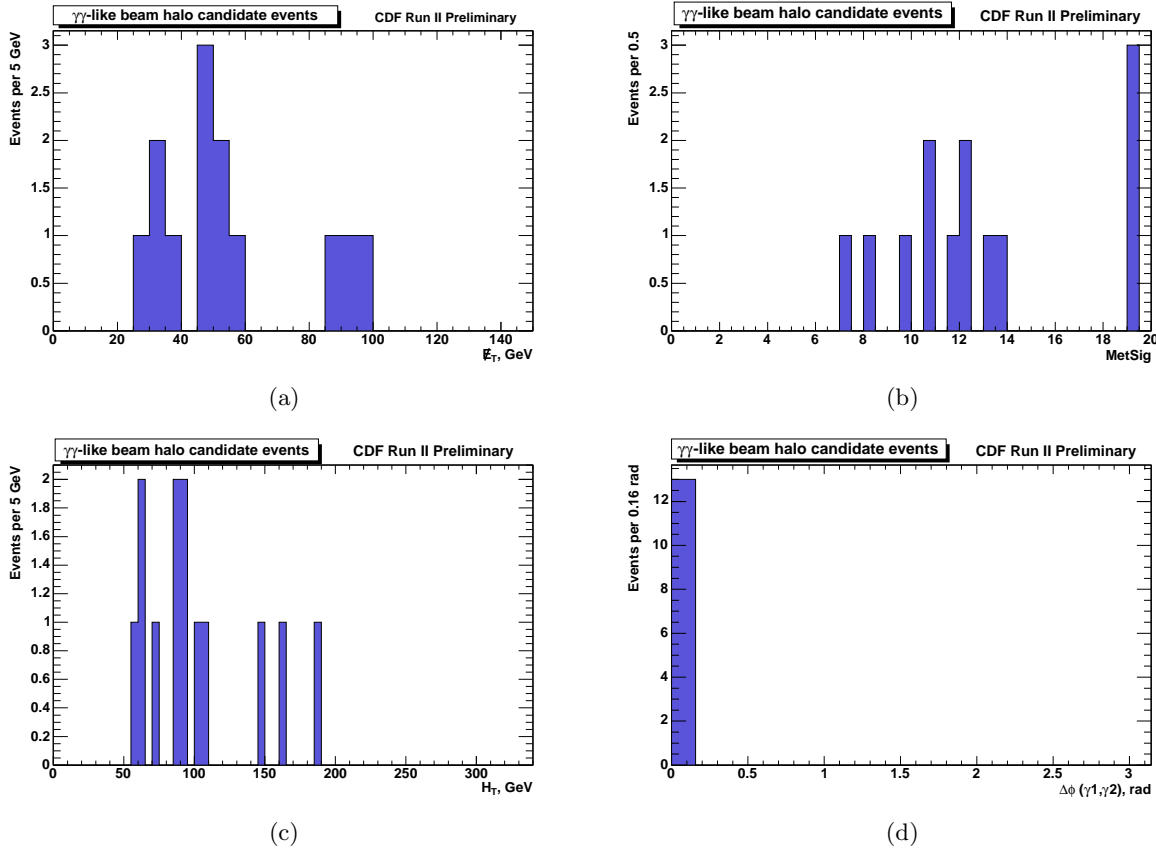


Figure 7: The \cancel{E}_T , \cancel{E}_T Significance, H_T and $\Delta\phi(\gamma_1, \gamma_2)$ distributions for the 13 events in the $\gamma\gamma$ beam halo enriched sample. Events are selected using the requirements in Table 13. As expected these events have large \cancel{E}_T Significance. They have small $\Delta\phi(\gamma_1, \gamma_2)$ by construction.

3.4.2 Cosmic Ray Events

Cosmic ray (C.R.) muon events fake the $\gamma\gamma + \cancel{E}_T$ signature via photon Bremsstrahlung as the muon traverses the magnet, or by catastrophic interaction with the EM calorimeter. In addition to using the EMTiming system to remove contamination due to cosmic rays (see Table 7), we also use it to evaluate the remaining contribution after the kinematic cuts. We select a cosmic ray enriched sample of $\gamma\gamma + \cancel{E}_T$ candidate events, by selecting events: two photons passing the loose photon ID cuts in Table 12, but failing the timing cuts. Specifically at least one of the photon candidate must have $T_\gamma > 25$ ns. That way we take into account all cosmic ray sources; both photons from the the same cosmic ray, both photons from different cosmic rays and one photon from a cosmic ray and one from collision. To increase the sample statistics events are not required to pass our vertex cut ($|Z_{vx}| < 60$ cm), which we correct for in our sample estimate, using similar techniques in the previous section for B.H.. The full set of requirements are given in Table 14. This gives us a pure sample of 40 C.R. events ($N_{\text{control}}^{\text{CR}}$). We use all 40 events as a template for the \cancel{E}_T , \cancel{E}_T Significance, H_T and $\Delta\phi(\gamma_1, \gamma_2)$ distributions as shown in Figure 8, from which we will use as a rejection fraction, $R_{\text{kinematic}}^{\text{CR}}$.

DIPHOTON_12, DIPHOTON_18, PHO_50 or PHO_70 trigger
Two photons passing the loose photon ID cuts in Table 12
No vertex requirements
$ T_{\gamma_1} $ or $ T_{\gamma_2} > 25$ ns

Table 14: Summary of cuts to select cosmic ray enriched sample. A total of 40 events pass these requirements.

To estimate the expected number of C.R. events in the signal region, we take

$$N_{\text{signal}}^{\text{CR}} = N_{\text{control}}^{\text{CR}} \cdot R_{\text{kinematic}}^{\text{CR}} \cdot R_{\text{ID,VX}}^{\text{CR-window}[25,120]} \cdot R_{\Delta T}^{\text{CR}} \quad (15)$$

where $R_{\text{kinematic}}^{\text{CR}}$ is the rejection factor for kinematic requirements and is used to estimate the rate at which C.R. events pass these requirements, and $R_{\text{ID,VX}}^{\text{CR-window}[25,120]}$ is the rejection factor to estimate the rate at extrapolating C.R. events that either photon passes the photon ID cuts and the vertex requirements but the timing cuts in control timing window [25,120] ns into signal timing window $[4\sigma_T, -4\sigma_T]$ ns. The $R_{\Delta T}^{\text{CR}}$ is the rejection factor to estimate the rate at which C.R. events pass a cut on $\Delta T_{\gamma\gamma}$ between arrival time of two photons. The first rejection factor, $R_{\text{kinematic}}^{\text{CR}}$, is estimated by

$$R_{\text{kinematic}}^{\text{CR}} = \frac{N_{\text{kinematic}}^{\text{CR-control}}}{N_{\text{control}}^{\text{CR}}} \quad (16)$$

where $N_{\text{kinematic}}^{\text{CR-control}}$ is the number of events in the control sample that pass the final kinematic cuts. To estimate the second rejection factor, $R_{\text{ID,VX}}^{\text{CR-window}[25,120]}$, we count the number of events in a control region timing window [25,120] ns that pass the photon ID and vertex requirements and extrapolate into the signal region timing window $[-4\sigma_T, 4\sigma_T]$ ns, where $\sigma_T = 1.665$ ns, assuming flat timing distribution. Thus, the $R_{\text{ID,VX}}^{\text{CR-window}[25,120]}$ is estimated by

$$R_{\text{ID,VX}}^{\text{CR-window}[25,120]} = \frac{N_{\text{ID,VX}}^{\text{CR-window}[25,120]}}{N_{\text{control}}^{\text{CR}}} \times \frac{(4 \cdot \sigma_T - (-4 \cdot \sigma_T))\text{ns}}{(120 - 25)\text{ns}}$$

$$= \frac{7}{40} \times \frac{(4 \times 1.665 - (-4 \times 1.665))\text{ns}}{(120 - 25)\text{ns}} = 0.025 \quad (17)$$

where $N_{\text{ID},\text{VX}}^{\text{CR}-\text{window}[25,120]} = 7$ is the number of events that pass the photon ID and vertex requirement where either photon has the arrival time in the range $25 \text{ ns} < T_\gamma < 120 \text{ ns}$. This evaluation is based on the fact that the cosmics arrival time is independent of the collision time as shown in Figure 9. The last rejection fraction, $R_{\Delta T}^{\text{CR}}$, for the $\Delta T_{\gamma\gamma}$ cut between arrival time of two photons, is given by

$$R_{\Delta T}^{\text{CR}} = \frac{N_{\Delta T}^{\text{CR-ID,VX}}}{N_{\text{control}}^{\text{CR}}} = \frac{1}{40} \quad (18)$$

where $N_{\Delta T}^{\text{CR-ID,VX}} = 1$ is the number of events that pass the photon ID and vertex cuts with $\Delta T_{\gamma\gamma} < 5 \cdot \sigma_{\Delta T} \text{ ns}$ between arrival times of both photons, where $\sigma_{\Delta T} = 1.021 \text{ ns}$ ⁴. Thus, the final expected number of C.R. events in the signal region that pass the final kinematic cuts is given by

$$\begin{aligned} N_{\text{signal}}^{\text{CR}} &= N_{\text{control}}^{\text{CR}} \cdot R_{\text{kinematic}}^{\text{CR}} \cdot R_{\text{ID,VX}}^{\text{CR}-\text{window}} \cdot R_{\Delta T}^{\text{CR}} \\ &= 40 \cdot \frac{N_{\text{kinematic}}^{\text{CR-control}}}{40} \cdot 0.025 \cdot \frac{1}{40} \\ &= N_{\text{kinematic}}^{\text{CR-control}} \cdot (0.001) \\ &= N_{\text{kinematic}}^{\text{CR-control}} \cdot \text{SF}_{\text{CR}} \end{aligned} \quad (19)$$

where we take $\text{SF}_{\text{CR}} = 0.001 \pm 0.001$. (stat. only).

The uncertainties are dominated by statistical uncertainty on the number of identified cosmics events.

After estimating beam halo and cosmic ray backgrounds, the expected kinematic distributions for combined non-collision backgrounds in the presample are shown in Figure 10.

⁴We used $4 \cdot \sigma_{\Delta T}$, but found no event, so extend it to $5 \cdot \sigma_{\Delta T}$.

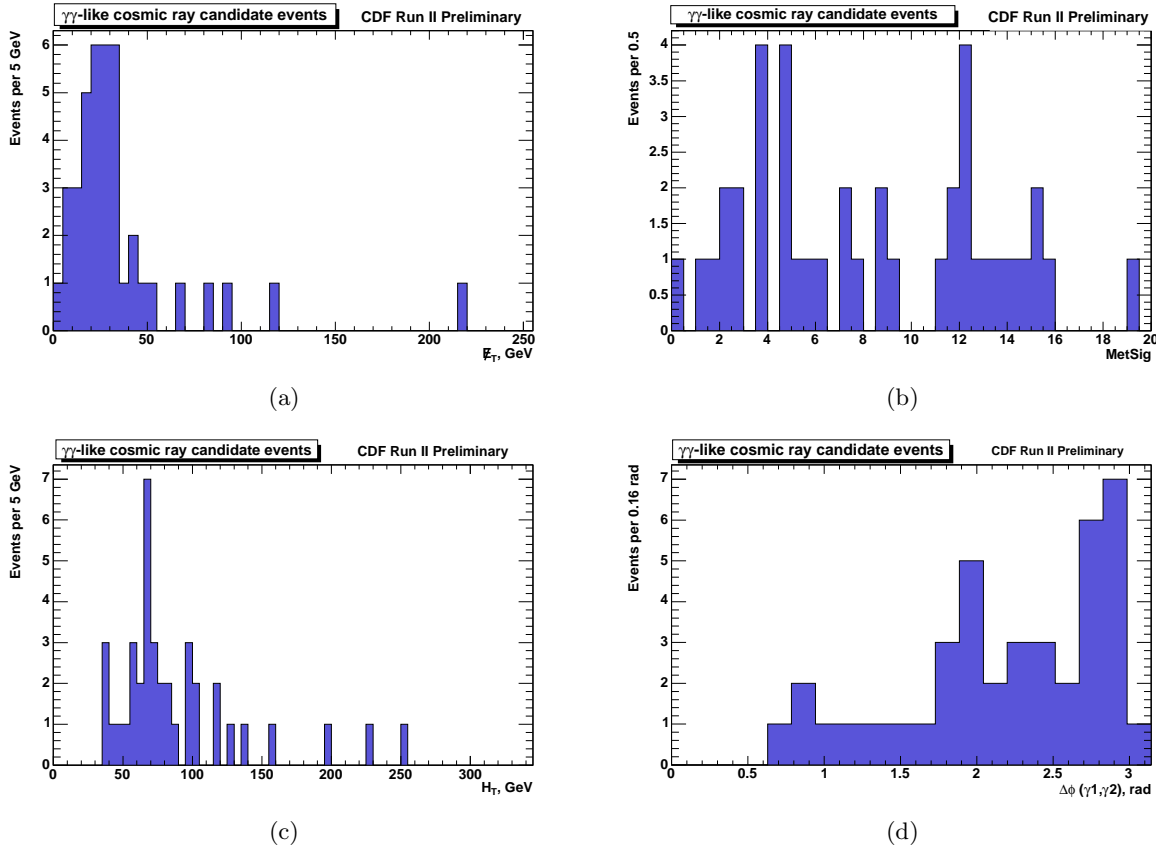


Figure 8: The \mathbb{E}_T , \mathbb{E}_T Significance, H_T and $\Delta\phi(\gamma_1, \gamma_2)$ distributions for the 40 events in the $\gamma\gamma$ events in the cosmic ray enriched sample. Events are selected using the requirements in Table 14.

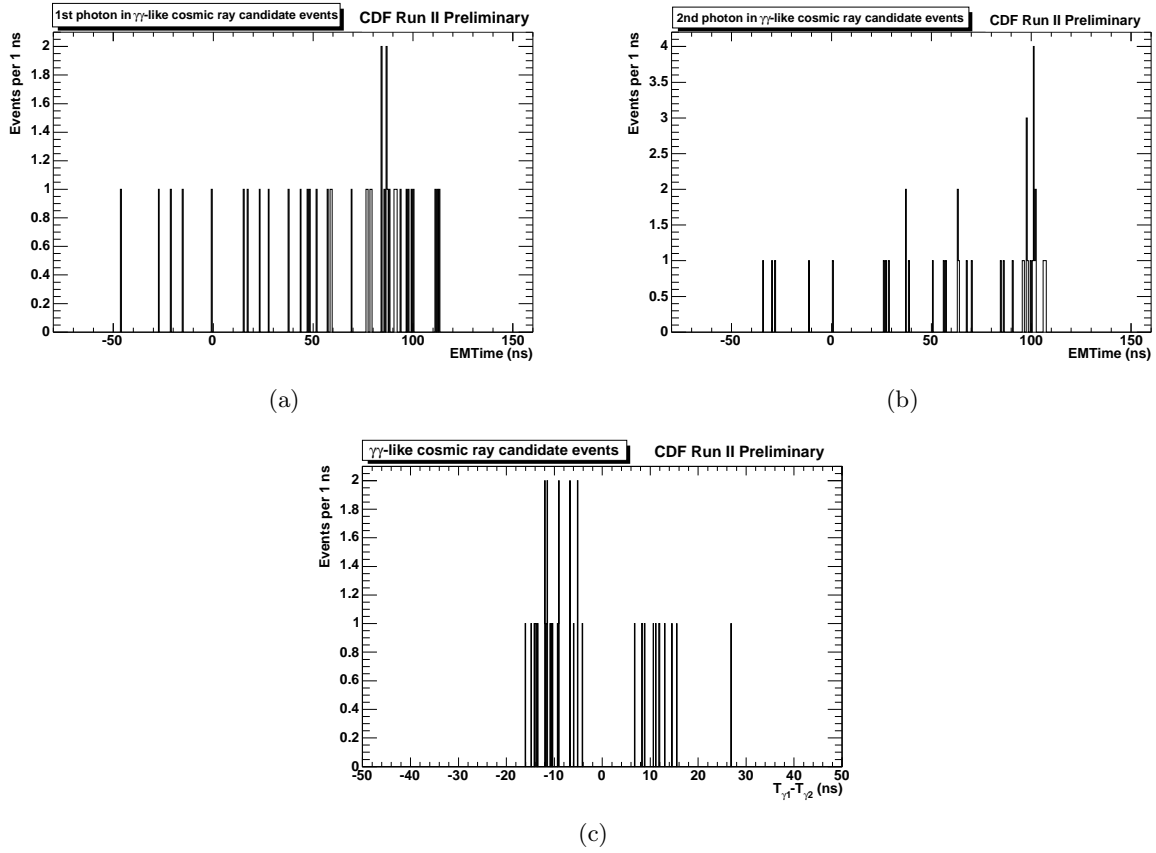


Figure 9: (a) and (b) show the EMTiming distributions for the first and second photons, respectively, for the 40 observed $\gamma\gamma$ -like cosmic events selected using the requirements in Table 14. (c) shows the $\Delta T_{\gamma\gamma} = T_{\gamma 1} - T_{\gamma 2}$ between the arrival times of the two photons.

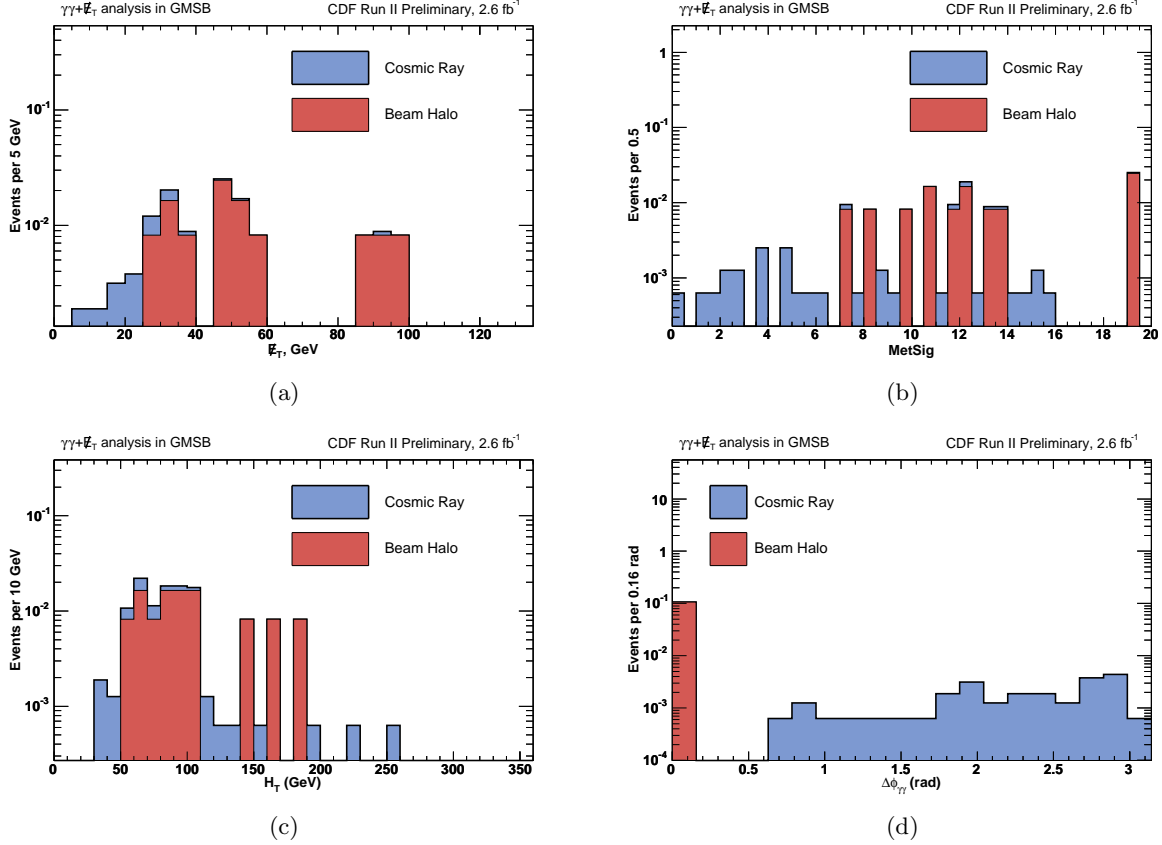


Figure 10: The non-collision background predictions after the preselection requirements, but with B.H. and C.R. normalized by SF_{BH} and SF_{CR} respectively. (a), (b), (c) and (d) show the \cancel{E}_T , \cancel{E}_T Significance, H_T and $\Delta\phi(\gamma_1, \gamma_2)$ distributions respectively.

3.5 Background Summary

After estimating all the backgrounds, the expected kinematic distributions, normalized to expectations for all combined backgrounds of QCD, electroweak and non-collision for the presample are shown in Figure 11. A number of caveats are in order about these plots. For example, the QCD contributions in (a), (b), and (c) are calculated using the pseudo experiments based on the presample. Thus, the predictions and data are highly correlated. In Figure (d), the agreement is almost exact since there is no variation in the $\Delta\phi(\gamma_1, \gamma_2)$ in the pseudoexperiments for the QCD contribution. However, the \cancel{E}_T Significance in Figure (b) shows the clear separation between the QCD and EWK backgrounds showing the power of our background estimation techniques and our understanding level of the data sample.

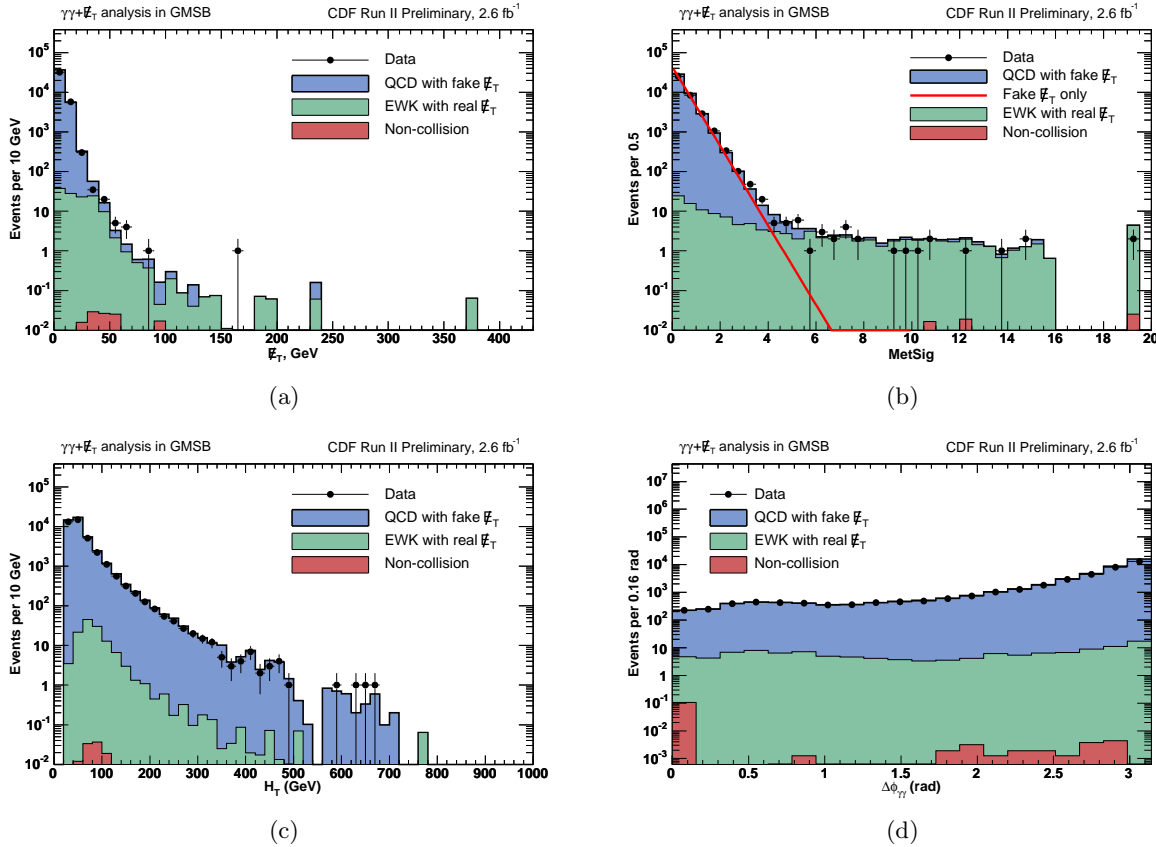


Figure 11: The \cancel{E}_T , \cancel{E}_T Significance, H_T and $\Delta\phi(\gamma_1, \gamma_2)$ predictions after the preselection requirements along with the data. Figure (b) includes predictions for all the backgrounds along with the perfect prediction of fake \cancel{E}_T only indicated with the red line, which has a simple *a priori* distribution of $dN/dx = N_{\text{event}} \times \ln(10) \times 10^{-x}$. Also, events at large \cancel{E}_T Significance in Figure (b) are overflow bins.

4 Acceptances for GMSB Models

In this section we describe the MC simulation of the GMSB model, and how we estimate our signal acceptance. For the purpose of this analysis we consider a GMSB model with the following parameters fixed on the minimal-GMSB Snowmass slope constraint (SPS 8) that is commonly used [17, 16]:

$$N = 1, \quad M_m/\Lambda = 2, \quad \tan\beta = 15, \quad \mu > 0.$$

This reduces the six free parameters in Table 1 to two which we take as the $\tilde{\chi}_1^0$ mass and lifetime. To simulate events and we use the PYTHIA event generator and use *cdfSim* of *cdfsoft* release 6.1.4 [11, 36] with the default settings, modified for the simulation of the EMTiming system (see App. B in Ref. [37]). We simulate the full GMSB model with the setting MSEL=39 with the masses calculated with ISASUGRA [38]. We use the detector calibrations of p1 to p13 for all MC samples with tune-A and Min-Bias to properly simulate effects due to vertex swap and \cancel{E}_T cleanup cut. Each sample contains 133,330 events which yields a statistical uncertainty of $\sim 1\%$ since the probability for signal events to pass our final kinematic cuts is $\sim 8\%$. For our analysis we only consider $\tilde{\chi}_1^0$'s lifetimes up to 2 ns since *cdfSim* does not simulate χ_{CES}^2 correctly for a high incident angle photons from higher lifetime $\tilde{\chi}_1^0$'s [37]. Also the next generation delayed photon analysis will deal with high lifetimes.

The total event acceptance, $A_{\text{Signal MC}}$, is used when calculating the cross section limits, and is quantitatively defined by:

$$A_{\text{Signal MC}}(\%) = \frac{N_{\text{events}}^{\text{passing all cuts}}}{N_{\text{events}}^{\text{total produced}}} \cdot \quad (20)$$

The breakdown of events passing each of the selection cuts for an example GMSB point at $m(\tilde{\chi}_1^0) = 140$ GeV and $\tau(\tilde{\chi}_1^0) = 0$ ns is shown in Table 15. For completeness we have included the results for the final event selection, determined in Section 6.

Requirement	Events passed	$A_{\text{Signal MC}}(\%)$ ($m(\tilde{\chi}_1^0) = 140$ GeV and $\tau(\tilde{\chi}_1^0) = 0$ ns)
Sample events	133330	100.00
Two EM Objects and $ z_{\text{vertex}} < 60$ cm	124771	93.6
Photon fiducial & Standard ID cuts	18270	13.7
Phoenix Rejection & PMT cuts	17625	13.2
Beam Halo and Cosmic Rejection cuts	17612	13.2
Vertex Swap and \cancel{E}_T Cleanup cuts	17049	12.8
\cancel{E}_T Significance > 3	12610	9.5
$H_T > 200$ GeV	11913	8.9
$\Delta\phi(\gamma_1, \gamma_2) < \pi - 0.35$	10395	7.8

Table 15: Summary of the event reduction for a GMSB example point in the $\gamma\gamma + \cancel{E}_T$ final state. We have included the final, optimized cuts for completeness.

5 Estimation of the Systematic Uncertainties

Since we estimate the sensitivity of the search to be equal to the expected 95% C.L. cross section limits, we need the uncertainties for the trigger, luminosity, background and acceptance. As mentioned in Section 2, with our combination of triggers we take a trigger efficiency of 100% with negligible error. The systematic uncertainty on the luminosity is taken to be 6% with major contributions from the uncertainties on the CLC acceptance from the precision of the detector simulation and the event generator [39]. The systematic uncertainty on the background in the signal region is determined from our understanding of both the collision and non-collision sources, as described in Section 3. The background uncertainty is evaluated for every set of cuts in the optimization procedure. The acceptance and cross section uncertainties are estimated in the subsections below. The results are summarized in Table 16 for an example GMSB point of $m(\tilde{\chi}_1^0) = 140$ GeV and $\tau(\tilde{\chi}_1^0) = 0$ ns. All uncertainties are consistent with the GMSB diphoton analysis in Ref. [17] unless otherwise noted. We take the systematic uncertainty to be constant for all masses.

Factor	Relative Systematic Uncertainty (%)
Acceptance:	
Diphoton ID and Isolation	5.4
ISR/FSR	3.9
JES	1.6
\cancel{E}_T Significance parameterizations	0.7
PDFs	0.4
Total	6.9
Cross section:	
PDF	7.6
Renormalization scale (Q^2)	2.6
Total	8.0

Table 16: Summary of the systematic uncertainties on the acceptance and production cross section for an example GMSB point at $m(\tilde{\chi}_1^0) = 140$ GeV and $\tau(\tilde{\chi}_1^0) = 0$ ns. For the optimization we combine in quadrature and take a 10.6% uncertainty on the acceptance.

5.1 Acceptance Uncertainties

There are a number of effects that can cause our estimate of the acceptance to be systematically mis-estimated. We identify them here, by order of decreasing magnitude, and explain how they are estimated. The dominant uncertainty on the acceptance is the photon ID and isolation.

5.1.1 Photon ID and Isolation Efficiencies

The photon ID and Isolation variables are imperfectly modeled in *cdfSim*. This has been studied in detail elsewhere. We take a systematic uncertainty of 1.8% for the photon ID and 2.0% for isolation efficiencies as described in Ref. [40, 41] in quadrature for a total of 2.7% uncertainty per photon. Since there are two photons we take the total systematic uncertainty to be $2 \times 2.7\% = 5.4\%$. This represents an improvement over the 202 pb^{-1} result due to improved understanding of the detector[17].

5.1.2 ISR/FSR (Initial and Final State Radiation)

Initial state radiation (ISR) caused by a gluon radiating from an incoming parton or final state radiation (FSR) from an outgoing jet can both make the E_T spectrum of the final state particles softer than expected without radiation. This can cause the photon, the jets or the \cancel{E}_T to be systematically more or less likely to pass the kinematic requirements. The effect carries a non-negligible theoretical uncertainty and is estimated using the standard CDF procedure by varying the Sudakov parameters as described in [42]. Doing so we find a variation in the acceptance, taken to be the systematic uncertainty, of 3.9%.

5.1.3 JES (Jet Energy Scale)

Since we allow jets with a corrected $E_T > 15$ GeV to be counted in our H_T and \cancel{E}_T *Significance* calculations in our set of events we have studied the change in acceptance if the jet energy is mismeasured. The following effects are taken into account: relative jet energy, underlying event, multiple interaction, absolute energy scale, out-of-cone and splash-out. The standard procedure at CDF [34] varies each correction factor independently by $\pm 1\sigma$. The resulting variation on the acceptance is $\pm 1.6\%$.

5.1.4 \cancel{E}_T *Significance* parameterization and calibration

The \cancel{E}_T *Significance* calibrations and unclustered-energy parameterizations are slightly different for data and MC (See Figs. 10 and 16 in Ref. [21]). To estimate the magnitude of this uncertainty on the acceptance, we compare the acceptance using the most different sets and find the uncertainty on the acceptance to be 0.7%.

5.1.5 PDFs (Structure Functions)

In an event where proton and antiproton bunches collide it is mostly a single subparticle of the (anti-)proton, a parton (quark or gluon), that participates in the hard collision and produces a high center-of-mass energy event. The momentum fraction, described by parton distribution function (PDFs), that is carried by each of the partons in the proton or antiproton is not perfectly understood. It affects both the rate at which a process happens (the production cross section) and the kinematics of the outgoing final state particles (the acceptance of the event selection criteria).

To estimate the magnitude of this effect on the acceptance, for each simulated event the MC generator calculates the momentum fraction of the colliding parton using a standardized “PDF-set” by the CTEQ collaboration (CTEQ-5L) [43]. As only the newer PDF-set version CTEQ-6M contains 90% confidence intervals for each eigenvector, the total uncertainty is estimated using a standard procedure by reweighting the parton momenta of the original CTEQ-5L set and varying the PDFs using the uncertainties from CTEQ-6M as described in Ref. [43]. For the example GMSB point we get a relative uncertainty of $+0.3\% - 0.4\%$ [44] on the acceptance. We take the larger value to estimate the uncertainty conservatively.

5.2 Production Cross Section Uncertainties

The production cross section uncertainty is dominated by the uncertainty on the PDFs.

5.2.1 PDFs (Structure Functions)

Using the same methods in subsection 5.1.5, but considering the total production cross section calculation, for the example GMSB point we get a relative uncertainty of $+7.6\% - 7.3\%$ on the cross section. We take the larger value to estimate the uncertainty conservatively. This uncertainty is a little bit bigger than what we had in the delayed photon analysis ($\sim 5.9\%$ for $\tilde{\chi}_1^0$ mass=100 GeV) since our example point uses a heavier mass.

5.2.2 Q^2 (Renormalization Scale)

While the dominant GMSB production mechanisms are via electroweak processes (see Fig. 1), the probability that QCD processes occur via gluon emission and higher-order loops depend sensitively on the energy scale at which the process happens. In PYTHIA [11] events are generated using a fixed renormalized (q^2) scale of \hat{s} . However, the NLO cross section, which is calculated with PROSPINO2 [45], varies as a function of the renormalization scale. The variation of the NLO production cross section observed by changing the scale from $0.25 \cdot q^2$ to $4 \cdot q^2$ is calculated to be 2.6% for the example GMSB point.

5.3 Summary of the Systematic Uncertainties

All systematic errors are combined in quadrature to give 6.9% on the acceptance and 8.0% on the production cross section. These are combined in quadrature to give a total systematic uncertainty of 10.6%. The individual results are given in Table 16.

6 Optimization and Expected Limits

Now that the background estimation methods are determined and the signal acceptance is available for a given set of cuts, along with their uncertainties, an optimization procedure can be readily employed. Using only general cuts we can provide a robust and partially model independant search. We can then optimize that set of cuts before unblinding the signal region,

We choose to optimize for \cancel{E}_T *Significance*, H_T , and $\Delta\phi(\gamma_1, \gamma_2)$ cuts for following reasons⁵:

- \cancel{E}_T *Significance*:

As described in Section 3, this cut gets rid of most of the QCD background with fake \cancel{E}_T .

- H_T :

In GMSB production heavy gaugino pair-production dominates, and the gauginos decay to light, but high E_T , final state particles via cascade decays. Thus, GMSB signal has lots of H_T compared to SM backgrounds, which are dominated by QCD and Electroweak backgrounds which do not have lots of high E_T objects.

- $\Delta\phi(\gamma_1, \gamma_2)$:

Electroweak backgrounds with large H_T are typically a high E_T photon recoiling against $W \rightarrow e\nu$, which means the gauge boson decay is highly boosted. Thus, the two photon candidates in the final state are mostly back-to-back. Also, the high E_T diphotons with large H_T from QCD background are mostly back-to-back with fake \cancel{E}_T or wrong vertex. The $\Delta\phi(\gamma_1, \gamma_2)$ cut reduces both these backgrounds.

We optimize for all requirements simultaneously at each GMSB parameter point. Once we have the optimal values at each point we then check that if they are robust enough to be applied throughout the parameter space for simplicity. By estimating our sensitivity using the 95% C.L. expected cross section limits on GMSB models in the no-signal assumption, we find an optimal set of cuts before unblinding the signal region. We use the standard CDF cross section limit calculator [46] to calculate the limits, taking into account the predicted number of background events, the acceptance, the luminosity and their systematic uncertainties (see Section 5). We take

$$\sigma_{95}^{\text{exp}} = \sum_{N_{\text{obs}}=0}^{\infty} \sigma_{95}^{\text{obs}}(\text{cut}) \times \text{Prob}(N_{\text{obs}}, N_{\text{exp}} = \mu) \quad (21)$$

$$\text{RMS}^2 = \sum_{N_{\text{obs}}=0}^{\infty} (\sigma_{95}^{\text{obs}}(\text{cut}) - \sigma_{95}^{\text{exp}})^2 \times \text{Prob}(N_{\text{obs}}, N_{\text{exp}} = \mu) \quad (22)$$

where N_{obs} is the number of observed events in the pseudoexperiment, μ is the mean of the number of expected events as a function of the cuts and σ_{95}^{obs} denotes the cross section limit if N_{obs} were observed. Each are a function of the cut choices, so the expected cross section limit is also just a function of the cuts.

For each GMSB point the minimum expected cross section limit defines our set of optimal cuts. We chose \cancel{E}_T *Significance* > 3 , $H_T > 200$ GeV, $\Delta\phi(\gamma_1, \gamma_2) < \pi - 0.35$ rad as this maximizes the mass limit for $\tau = 0$. As an illustration of the optimization, Figures 13-(a), (c), and (e) show the expected cross section limit as a function of a cut while keeping all other cuts fixed at the optimized values. Indicated in green is the 8.0% uncertainty-band on the production cross section. In yellow we show the expected statistical variation in the cross section limit using the data in Table 17 and the RMS definition in Eq. 22. We decided to use a single set of cuts before we open the box based

⁵Many other cuts were considered, including \cancel{E}_T , $\Delta\phi(\gamma_1, \cancel{E}_T)$, $\Delta\phi(\gamma_2, \cancel{E}_T)$, $\Delta\phi(\text{jet}, \cancel{E}_T)$, $E_T^{\gamma 1}$, $E_T^{\gamma 2}$ and N_{jets} (number of jets), but these yield negligible gain and add additional systematic uncertainties.

with the expectation that they will yield the largest expected exclusion region with our significant loss of sensitivity to lower mass scenarios.

With these cuts we predict 1.23 ± 0.38 background events with 0.77 ± 0.30 from SM electroweak sources with real \cancel{E}_T , 0.46 ± 0.24 from QCD with fake \cancel{E}_T and $0.001^{+0.008}_{-0.001}$ from non-collision. Table 18 shows the raw numbers and calculations for the individual electroweak background sources after the optimal cuts. They are summarized in Table 19. Note that the electroweak global scale factor was calculated for each different set of cuts ($0 \leq \cancel{E}_T \text{ Significance} \leq 10$ in steps of 1, $0 \leq H_T \leq 400$ GeV in steps of 25 GeV, and $2.4 \leq \Delta\phi(\gamma_1, \gamma_2) \leq 3.14$ rad in steps of 0.05 rad) and its distribution is shown in Figure 12. The dominant electroweak contributions are $Z \rightarrow \mu\mu$ and $Z \rightarrow \nu\nu$ which produce a total of 0.19 ± 0.10 and 0.11 ± 0.03 events respectively. More details on the QCD background contributions are given in Tables 20. The QCD background is dominated by gaussian fluctuations in the \cancel{E}_T , estimated using the *Met Model* to have a rate of 0.40 ± 0.20 events. The non-collision background calculations are shown in Table 21 and are dominated by cosmics which has a rate of 0.001 ± 0.001 . Table 22 provides the final summary.

Table 23 shows the expected cross section limits, acceptance and production cross section of each GMSB point simulated, along with the predicted backgrounds. Figures 13-(b), (d), and (f) show the distributions of each optimization variable normalized to the number of expected events, after applying all optimized cuts. We compare the background distribution before unblinding the signal region and the expected signal in the signal region for an example GMSB point at $m(\tilde{\chi}_1^0) = 140$ GeV and $\tau(\tilde{\chi}_1^0) = 0$ ns. Taking into account the errors we expect an acceptance of $(7.80 \pm 0.83)\%$. In the next section, we unblind the signal region and set limits on GMSB models.

We note that we do not do a separate optimization for non-zero lifetimes. Rather we simply estimate the sensitivity of our analysis to these scenarios for lifetimes up to 2 ns. The expected results are given in Table 23.

N_{obs}	Probability	$\sigma_{obs}(N)$ (fb)
0	0.346	15.1
1	0.367	21.0
2	0.195	27.6
3	0.069	34.5
4	0.018	41.6
5	0.004	48.6

Table 17: The 95% C.L. cross section limit as a function of the hypothetically observed number of events after optimization. The Poisson probability for this number of events is based on the background expectation of 1.06 events. The acceptance and production cross section are calculated for an example GMSB point of $m(\tilde{\chi}_1^0) = 140$ GeV/ c^2 and $\tau(\tilde{\chi}_1^0) = 0$ ns. The expected limit and its variation are calculated as shown in [46] with Eqs. 21 and 22. With these numbers we get an expected cross section limit of 21.6 fb and an RMS on the limit of 4.4 fb.

Background Source (Charged Leptons)	SF _i	EWK $\gamma\gamma + \cancel{E}_T$ signal		0.8 < E/p < 1.2 for e γ		0.0 < E/p < 2.0 for e γ	
		MC Events	N _{signal,<i>i</i>} ^{EWK-MC} · SF _i	MC Events	N _{eγ,signal,<i>i</i>} ^{MC} · SF _i	MC Events	N _{eγ,signal,<i>i</i>} ^{MC} · SF _i
W(e) + γ	0.064	1	0.064±0.064	83	5.270±0.578	99	6.286±0.632
W(μ) + γ	0.060	0	0.00±0.060	0	0.00±0.060	0	0.00±0.060
W(τ) + γ	0.061	1	0.061±0.061	3	0.183±0.105	3	0.183±0.105
Z(e) + γ	0.004	3	0.012±0.007	64	0.252±0.031	76	0.299±0.034
Z(μ) + γ	0.004	35	0.138±0.023	5	0.020±0.009	8	0.032±0.011
Z(τ) + γ	0.004	25	0.099±0.020	93	0.368±0.038	129	0.511±0.045
W(e) + γ no ISR/FSR	0.210	0	0.00±0.035	4	0.84±0.42	5	1.05±0.47
W(μ) + γ no ISR/FSR	0.308 (0.699)	0	0.00±0.051	0	0.00±0.699	0	0.00±0.699
W(τ) + γ no ISR/FSR	0.296	0	0.00±0.049	0	0.00±0.296	0	0.00±0.296
Z(e) + γ no ISR/FSR	0.056	0	0.00±0.056	1	0.056±0.056	1	0.056±0.056
Z(μ) + γ no ISR/FSR	0.088 (0.126)	0	0.00±0.088	0	0.00±0.126	0	0.00±0.126
Z(τ) + γ no ISR/FSR	0.039	1	0.039±0.039	1	0.039±0.039	1	0.039±0.039
t \bar{t} (incl.)	0.0023	25	0.058±0.012	621	1.453±0.058	739	1.729±0.064
$\sum_{i=0}^n N_{\text{signal},i}^{\text{EWK-MC}} \cdot \text{SF}_i$			0.47±0.15				
$N_{e\gamma,\text{signal}}^{\text{MC}} = \sum_{i=0}^n N_{e\gamma,\text{signal},i}^{\text{MC}} \cdot \text{SF}_i$					8.49±1.06		10.18±1.11
$\frac{N_{e\gamma,\text{signal}}^{\text{Data}}}{N_{e\gamma,\text{signal}}^{\text{MC}}}$				12		16	
$\frac{N_{e\gamma,\text{signal}}^{\text{Data}}}{N_{e\gamma,\text{signal}}^{\text{MC}}}$				1.41±0.44		1.57±0.43	
The Final EWK Prediction $N_{\text{signal}}^{\text{EWK}}$ $= \sum_{i=0}^n N_{\text{signal},i}^{\text{EWK-MC}} \cdot \text{SF}_i \cdot \left(\frac{N_{e\gamma,\text{signal}}^{\text{Data}}}{N_{e\gamma,\text{signal}}^{\text{MC}}} \right)$				$=(0.47\pm0.15)\times(1.41\pm0.47)$			
				0.66±0.21±0.22 (Expected Rate±Stat±Sys)			

Table 18: The charged electroweak background calculations for the optimal cuts ($H_T > 200$ GeV, \cancel{E}_T Significance > 3.0 and $\Delta\phi(\gamma_1, \gamma_2) < \pi - 0.35$). The SF_i scale factors are taken from Table 11. All errors are stat. only unless noted otherwise. The final electroweak global scale factor with E/p variations is estimated for each different set of optimal cuts. Figure 12 shows the variation of the electroweak global scale factor for a number of different optimization cuts. We take a systematic uncertainty on the global electroweak scale factor of 0.47. These results are summarized in Table 19.

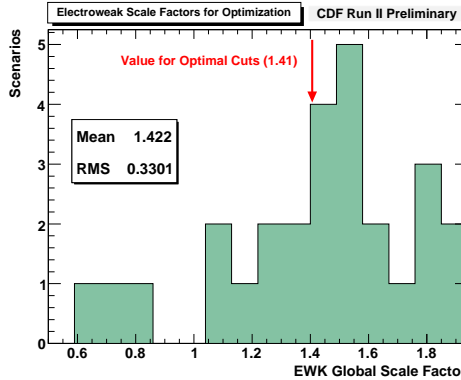


Figure 12: The electroweak global scale factor distributions for each different set of cuts considered in our optimization procedure. Note that our optimal point is near the mean of the distribution, consistent with no bias in the optimization and also consistent with uncertainties on the expectation from the E/p variation.

Background Source	Expected Rate \pm Stat \pm Sys
Charged leptons	
$W(l) + \gamma$	$0.176 \pm 0.149 \pm 0.059$
$Z(l) + \gamma$	$0.351 \pm 0.044 \pm 0.117$
$W(l) + \gamma$ no ISR/FSR	$0.0 \pm 0.111 \pm 0.0$
$Z(l) + \gamma$ no ISR/FSR	$0.055 \pm 0.096 \pm 0.018$
$t\bar{t}$	$0.082 \pm 0.017 \pm 0.027$
Neutral leptons	
$Z(\nu\nu) + \gamma\gamma$	$0.11 \pm 0.03 \pm 0.03$
EWK combined	$0.77 \pm 0.21 \pm 0.22$

Table 19: Summary of the scaled electroweak background estimations after optimization, taken from Table 18.

Background Source	Scale Factor	MC Events	<i>Met Model</i> Pred.	Normalized Pred.
			$N_{\text{signal}}^{\text{PATH-MC}}$	$N_{\text{signal}}^{\text{MM-MC}}$
Pathology	0.134 ± 0.007	1	0.527	$0.063 \pm 0.092 \pm 0.003$
QCD from <i>Met Model</i>				$0.40 \pm 0.20 \pm 0.10$
Total QCD				$0.46 \pm 0.22 \pm 0.10$

Table 20: Summary of the QCD background estimations after optimization. The normalized prediction from pathology is given by $N_{\text{signal}}^{\text{PATH}} = (N_{\text{signal}}^{\text{PATH-MC}} - N_{\text{signal}}^{\text{MM-MC}}) \cdot SF_{\text{QCD}}$ to avoid double counting the number of events from energy mis-measurements predicted by *Met Model*, where $N_{\text{signal}}^{\text{MM-MC}} = N_{\text{signal}}^{\text{noMetSig cut}} \cdot R_{\text{MetSig}}^{\text{exp}} = 527 \times 0.001$, using Eq.(3) described in Section 3.2.1.

Background Source	Total Rejection Fracton	Events Passed	Normalized Pred.
i	SF_i	$N_{\text{kinematic}}^{i-\text{control}}$	N_{signal}^i
Beam Halo	0.008 ± 0.008	0	$0.0 + 0.008 \pm 0.0$
Cosmic Rays	0.001 ± 0.001	1	$0.001 \pm 0.001 \pm 0.001$
Non-Collision			$0.001^{+0.008}_{-0.001} \pm 0.001$

Table 21: Summary of the non-collision background estimations after optimization. The normalized prediction of the beam halo (cosmic ray) is given by $N_{\text{signal}}^i = N_{\text{kinematic}}^{i-\text{control}} \cdot SF_i$, where $i=\text{BH}$ or CR , described in Section 3.4.

Background Source	Expected Rate \pm Stat \pm Sys
Electroweak	$0.77 \pm 0.21 \pm 0.22$
QCD	$0.46 \pm 0.22 \pm 0.10$
Non-Collision	$0.001^{+0.008}_{-0.001} \pm 0.001$
Total	$1.23 \pm 0.30 \pm 0.24$

Table 22: Summary of the combined background estimations after optimization. Note we have ignored the small asymmetric uncertainty in the total calculation.

$m_{\tilde{\chi}}$ (GeV/ c^2)	$\tau_{\tilde{\chi}}$ (ns)	Acceptance (%)	Background	σ_{95}^{exp} (fb)	σ_{95}^{obs} (fb)	$\sigma_{95}^{\text{prod}}$ (fb)
70	0	2.04 ± 0.43		81.92	57.20	999.9
70	1	1.85 ± 0.18		90.92	62.99	
70	2	1.41 ± 0.14		124.5	86.30	
80	0	4.29 ± 0.43		40.83	28.22	524.6
80	1	3.71 ± 0.37		45.59	31.51	
80	2	2.82 ± 0.28		60.02	41.48	
90	0	5.12 ± 0.51	Total: 1.23 ± 0.38 (0 observed)	32.76	22.65	286.8
90	1	4.42 ± 0.44		38.32	26.48	
90	2	3.48 ± 0.34		48.60	33.59	
100	0	6.74 ± 0.67	EWK: 0.77 ± 0.30 QCD: 0.46 ± 0.24	25.12	17.36	169.0
100	1	6.40 ± 0.64		26.46	18.29	
100	2	4.93 ± 0.49		34.25	23.67	
110	0	7.08 ± 0.71	Non-Collision: $0.001^{+0.008}_{-0.001}$	23.88	16.53	99.47
110	1	7.06 ± 0.71		23.95	16.54	
120	0	7.21 ± 0.72		23.50	26.24	58.38
120	2	5.64 ± 0.56		29.97	20.71	
130	0	7.86 ± 0.79		21.47	14.84	36.23
130	1	8.05 ± 0.80		20.98	14.49	
130	2	5.95 ± 0.60		28.44	19.67	
140	0	7.80 ± 0.78		21.64	15.11	22.97
140	1	7.87 ± 0.79		21.51	14.87	
140	2	6.08 ± 0.61		27.86	19.26	
150	0	7.95 ± 0.79		21.25	14.67	14.54

Table 23: The acceptance and expected cross section limits for various simulated GMSB points for the final selection requirements. For completeness we have included both the expected and observed number of events and cross section limits from Section 6. Note we use the same analysis for all masses and lifetimes up to 2 ns.

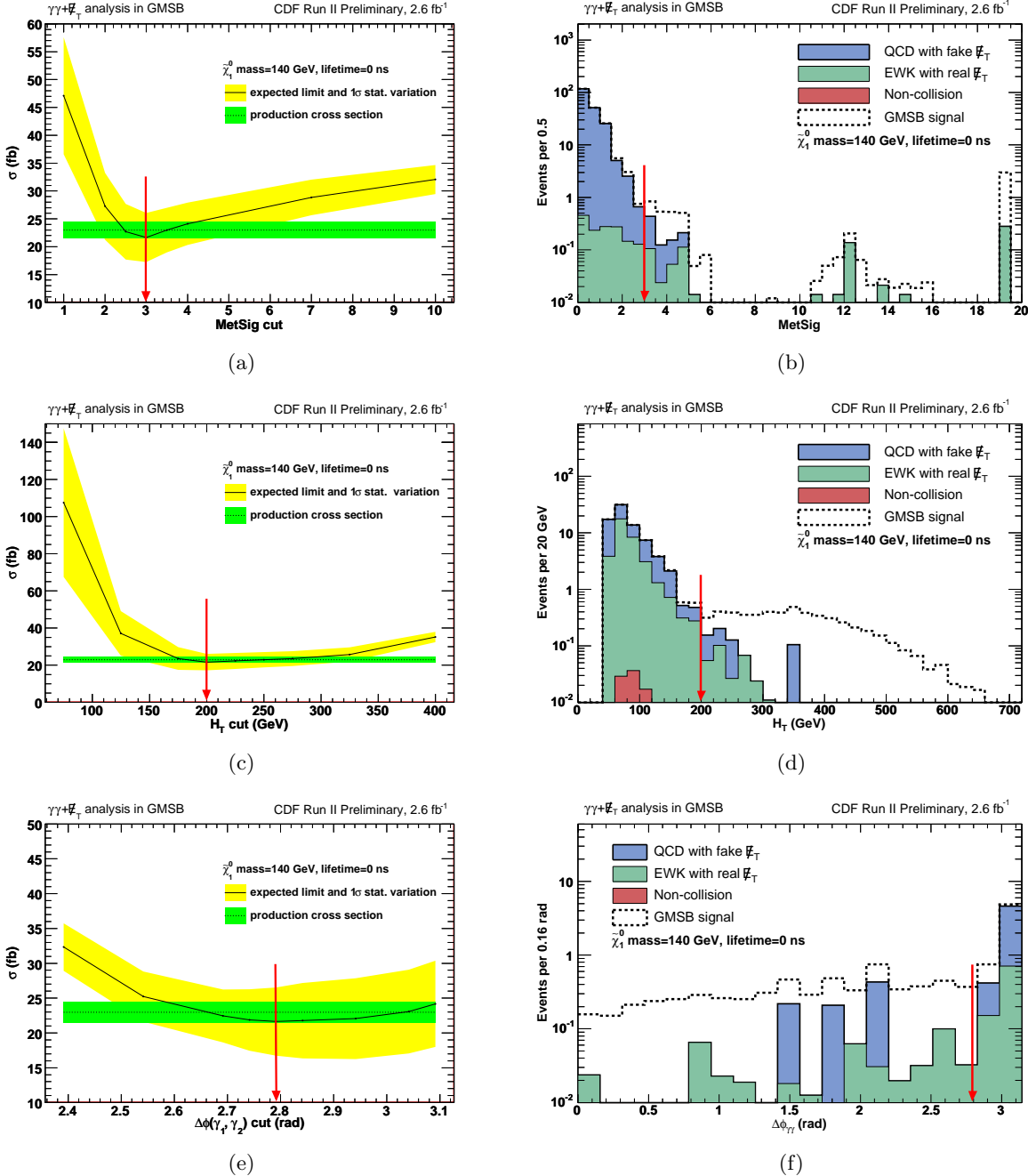


Figure 13: The expected 95% C.L. cross section limit as a function of the \cancel{E}_T Significance (a), H_T (c), and $\Delta\phi(\gamma_1, \gamma_2)$ (e) requirements for a GMSB example point ($m(\tilde{\chi}_1^0) = 140$ GeV and $\tau(\tilde{\chi}_1^0) = 0$ ns). All other cuts held at their optimized values. The optimal cut is where the expected cross section is minimized. Indicated in green is the 8.0% uncertainty-band for the production cross section (see Table 16) and in yellow is the RMS (See Eqn. 22). The N-1 predicted kinematic distributions after the optimized requirements are shown in Figure (b), (d), and (f).

7 Data, Cross Section Limits and Final Results

In this section we unblind the signal region, set cross section limits and show the exclusion regions as a function of neutralino mass and lifetime space for GMSB models.

7.1 The Data and Cross Section Limits

After all optimal cuts we open the box and observe no events in the signal region, consistent with the expectation of 1.23 ± 0.38 events. Figure 14 shows the kinematic distributions for the background and signal expectations along with the data. The data appears to be well modeled by the background prediction alone.

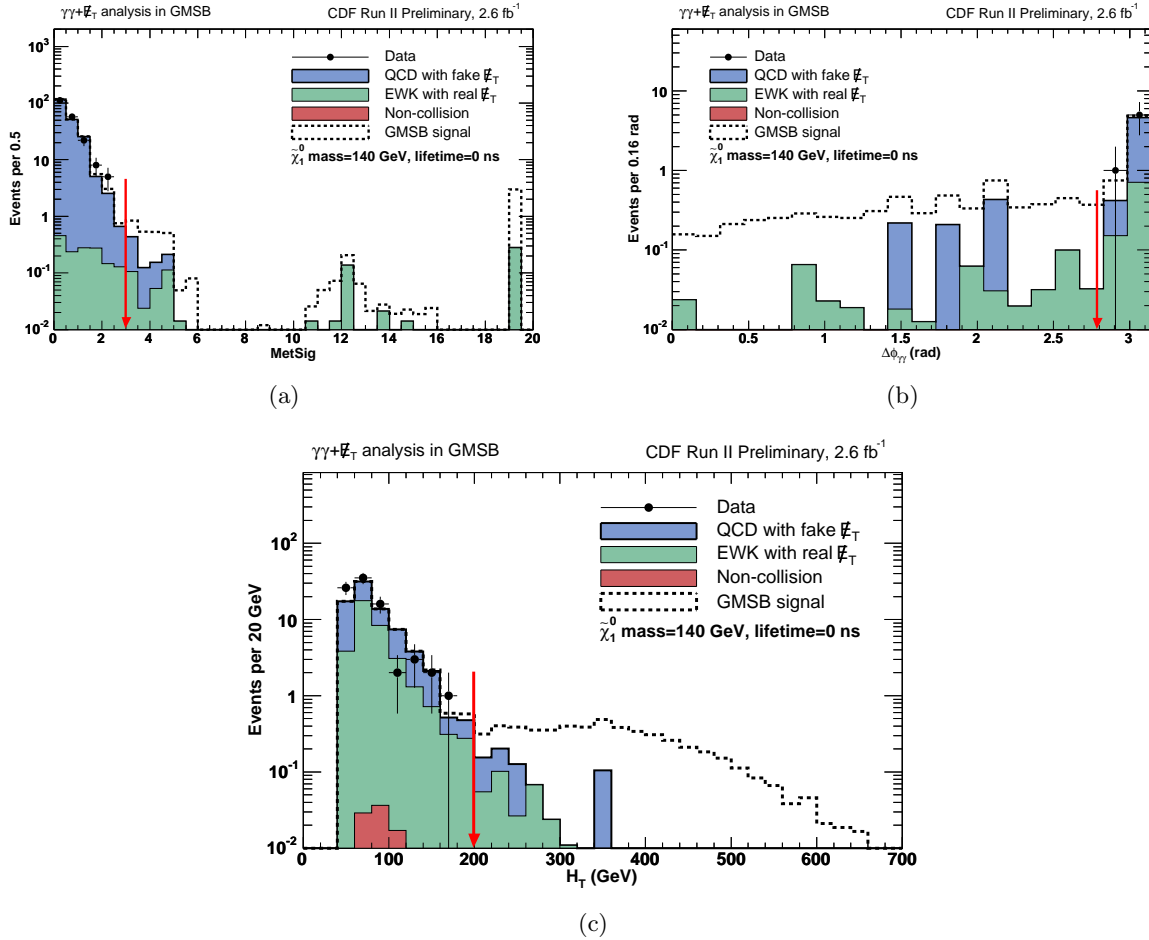


Figure 14: The same N-1 plots as Figure 13, but including the data. Each variable is plotted through the whole region while holding other variables at the optimal cuts. There is no evidence for new physics and the data is well modeled by backgrounds alone.

7.2 The GMSB Exclusion Region

Fig. 15 shows the predicted and observed cross section limits along with the NLO production cross section (see Table 16) as a function of $\tilde{\chi}_1^0$ mass at a lifetime of 0 ns and as a function of lifetime at a mass of 140 GeV/c^2 . Indicated in green is the 8.0% uncertainty-band on the production cross

section. In yellow we show the expected variation in the expected cross section limit using the data in Table 17 and the RMS definition in Eq. 22. Since the number of observed events is below expectations, the observed limits are slightly better than the expected limits. The $\tilde{\chi}_1^0$ mass reach, based on the predicted (observed) number of events is 141 GeV/c^2 (149 GeV/c^2), at a lifetime of 0 and 1 ns. We do not consider lifetimes above 2 ns for the reasons mentioned in Section 4 as well as the expectation that most of the parameter space in high lifetimes there should be excluded by searches in single delayed photon analysis [7, 19]. Fig. 16 shows the 95% C.L. NLO exclusion region as a function of mass and lifetime of $\tilde{\chi}_1^0$ using the fixed choice of cuts from the optimization for both for the predicted and observed number of background events. These limits extend the delayed photon results [19] to both masses and lifetime, at large masses, reaches well beyond those of DØ searches [18] and the limit from ALEPH/LEP [16], and are currently the world's best.

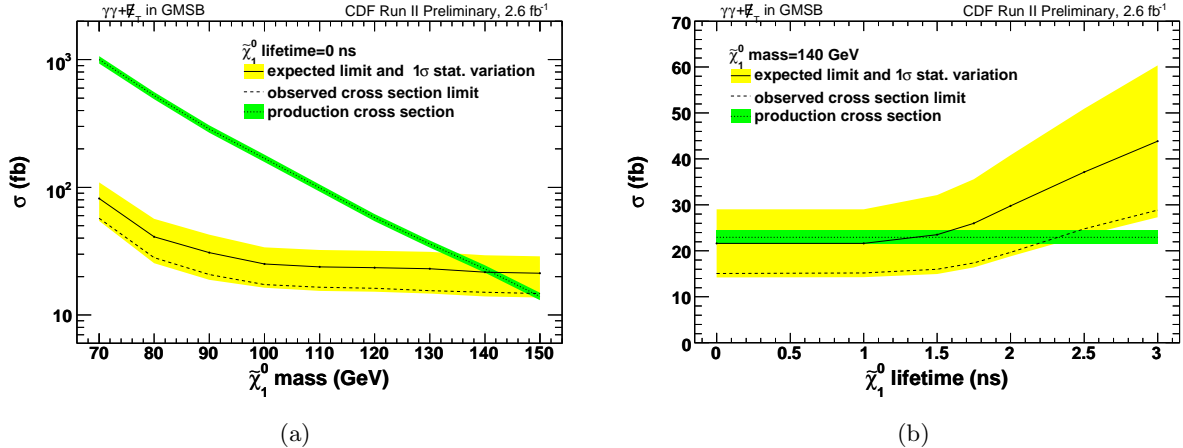


Figure 15: The predicted and observed cross section limits as a function of the $\tilde{\chi}_1^0$ mass at a lifetime of 0 ns (a) and as a function of the $\tilde{\chi}_1^0$ lifetime at a mass of 140 GeV/c^2 (b). Indicated in green is the 8.0% uncertainty-band for the production cross section (see Table 16), in yellow the RMS variation in the expected on the cross section limit.

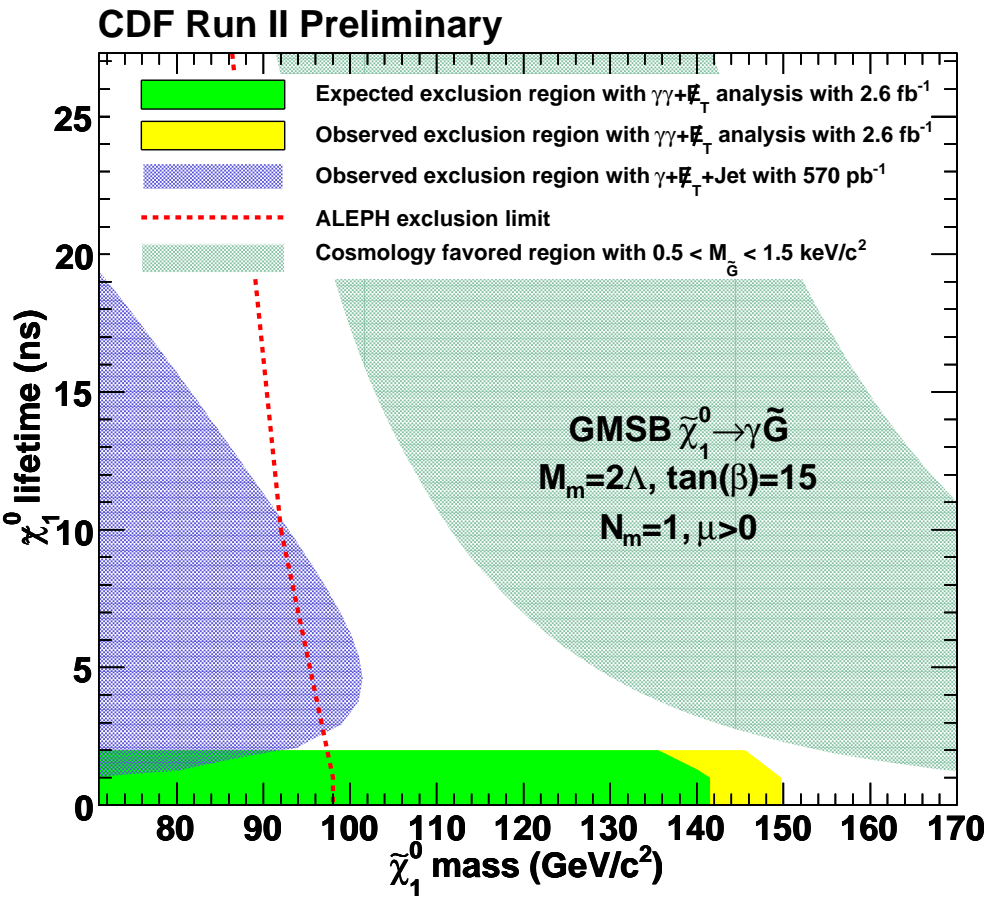


Figure 16: The predicted and observed exclusion region along with the limit from ALEPH/LEP [16] and the $\gamma + \cancel{E}_T + \text{jet}$ delayed photon analysis [19]. We have a mass reach of $141 \text{ GeV}/c^2$ (predicted) and $149 \text{ GeV}/c^2$ (observed) at the lifetime up to 1 ns. The blue shaded band shows the parameter space where $0.5 < m_{\tilde{G}} < 1.5 \text{ keV}/c^2$, favored in cosmologically consistent models [4].

8 Conclusions and Prospects for the Future

We have set limits on GMSB models using the $\gamma\gamma + \cancel{E}_T$ final state. Candidate events were selected based on the new \cancel{E}_T resolution model technique, the EMTiming system and a full optimization procedure. We found 0 event using 2.59 fb^{-1} of data in run II which is consistent with the background estimate of 1.23 ± 0.38 events from the Standard Model expectations. We showed exclusion regions and set limits on GMSB models with a $\tilde{\chi}_1^0$ mass reach of $149 \text{ GeV}/c^2$ at a $\tilde{\chi}_1^0$ lifetime of 0 ns. Our results extend the world sensitivity to these models.

To investigate the prospects of a search at higher luminosity we calculate the cross section limits assuming all backgrounds scale linearly with luminosity while their uncertainty fractions remain constant. Figure 17 shows the predicted exclusion region for a luminosity of 10 fb^{-1} . For higher lifetimes (above ~ 2 ns) the next generation delayed photon analysis will extend the sensitivity taken from Ref. [19] and then will combine these results for completeness.

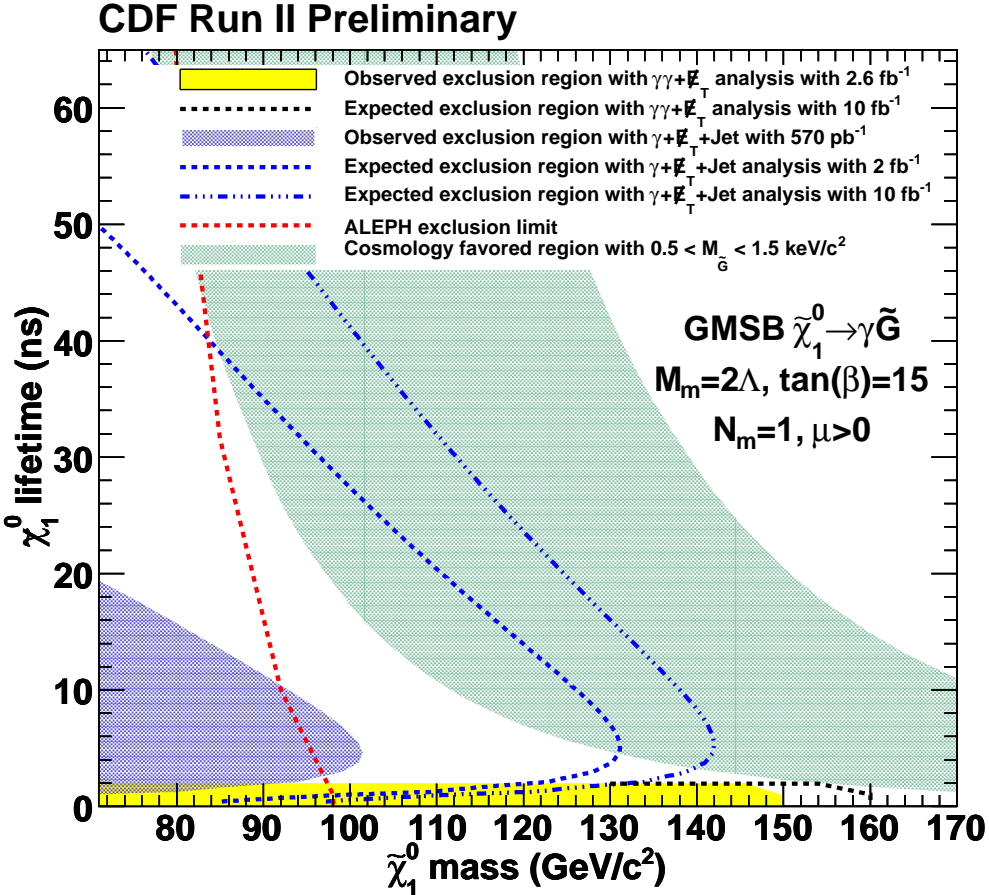


Figure 17: The black dashed line shows the prediction of the exclusion region limit after a scaling of the background prediction and the uncertainties for a luminosity of 10 fb^{-1} . The blue dashed lines show the prediction of the exclusion region limits from the delayed photon analysis for a luminosity of 2 fb^{-1} and 10 fb^{-1} respectively taken from Ref. [19].

A Appendix-I: Changes Since the 2 fb^{-1} Analysis

The results of the search for GMSB models in the $\gamma\gamma + \cancel{E}_T$ final state with 2 fb^{-1} of data were blessed on November 6, 2008 as described in version 2.0 of this note. In this section, we present a brief summary of changes and improvements compared to the previous measurement.

- Added p12 - p17 data (1.0 fb^{-1}), which has high instantaneous luminosity, and dropped p0 data (0.4 fb^{-1}), which has low instantaneous luminosity and no EMTiming information. This change has the following consequences:
 - Now all data has the EMTiming information. This allows for a single set of simple and efficient ways to remove cosmic rays and beam halo events. We dropped the old inefficient cosmic cuts.
 - Higher instantaneous luminosity increases the number of vertices per event, which results in larger contributions due to QCD wrong vertex. This, after re-optimization, is still negligible.
- We added the PHO_50 and PHO_70 triggers to recover loss in efficiency for χ^2_{CES} at high photon E_T . With these additions we take the trigger efficiency to be 100%. This leads to larger acceptances, but also larger backgrounds, in particular, larger electroweak backgrounds. However, these changes are again negligible after optimization.
- We realized we were not simulating the GMSB signal with Min-Bias. We now simulate the GMSB MC signal sample using PYTHIA with Tune-A and Min-Bias. These effects reduce the acceptance and thus the sensitivity from what was reported previously by a few percent.
- We switched back to using the vertex swap procedure to remove wrong vertex events and added the \cancel{E}_T cleanup cut to get rid of tri-photon events with a lost photon. We note this has inadvertently been done for the background estimations, but not for signal. Thus, our acceptance had been slightly overestimated relative to the backgrounds. Since the cuts are now part of the analysis they are correctly reported. We also confirmed that the vertex swap procedure and \cancel{E}_T cleanup cut help the sensitivity.
- We realized that the backgrounds reported had the \cancel{E}_T cleanup and wrong vertex cuts on them. Since we now use them explicitly, this requires no changes.
- We re-optimize after these changes and found that only the $\Delta\phi(\gamma_1, \gamma_2)$ cut needed to change from $\pi-0.15$ (2.99) to $\pi-0.35$ (2.79).
- We found that the formulae used to produce the cosmology favored region band in Figures 16 and 17 is incorrect. We now use Eq. (1) correctly to produce the band.

B Appendix-II: PRL Figures

Here we show the same plots as in the note, but with different style that go to PRL.

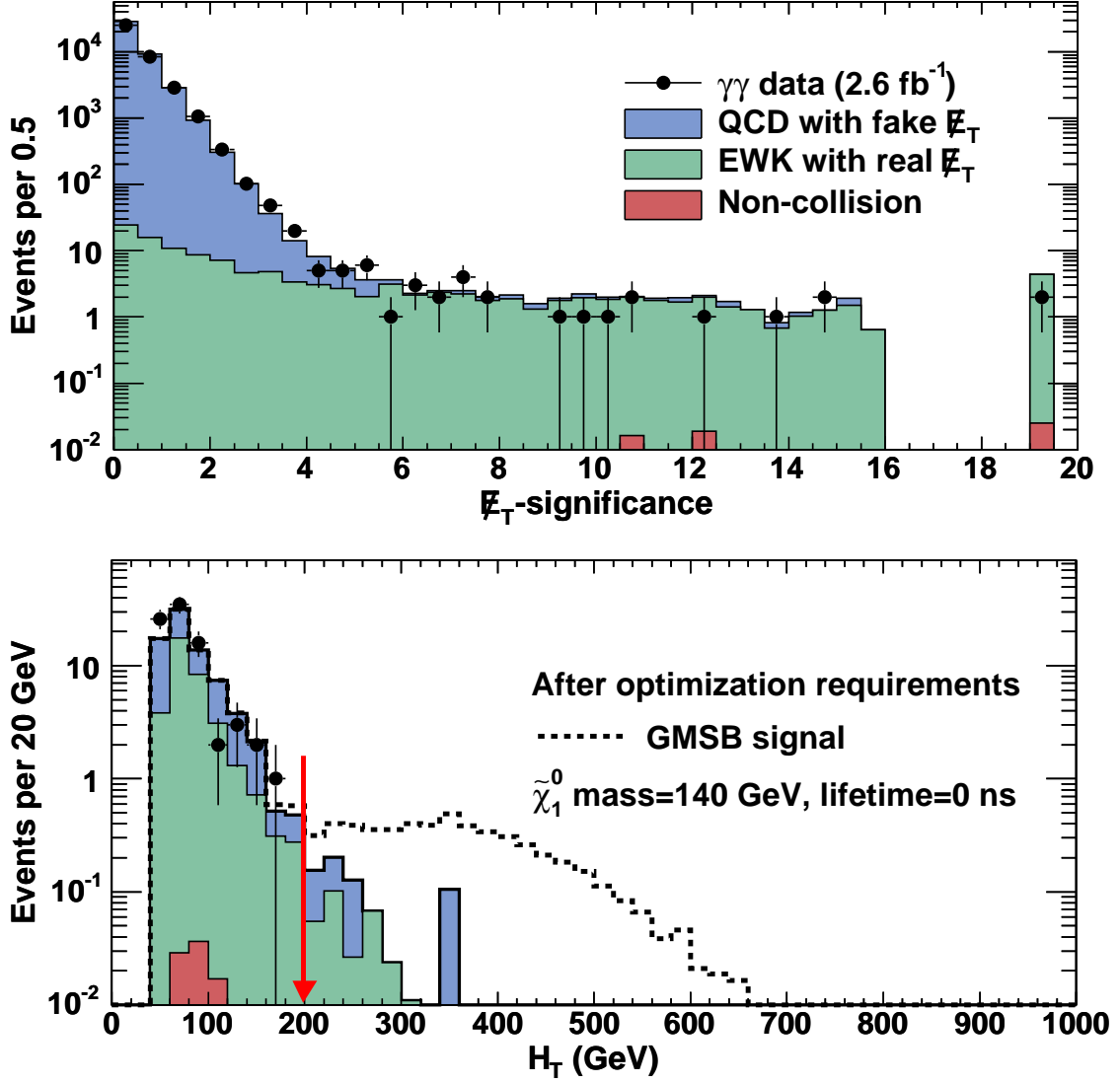


Figure 18: The top plot shows the MetSig prediction for the $\gamma\gamma$ sample after the preselection requirements along with the data, including predictions for all the backgrounds. The bottom plot shows the N-1 predicted H_T distribution after optimization, where the H_T is plotted through the whole region. There is no evidence for new physics and the data is well modeled by backgrounds alone.

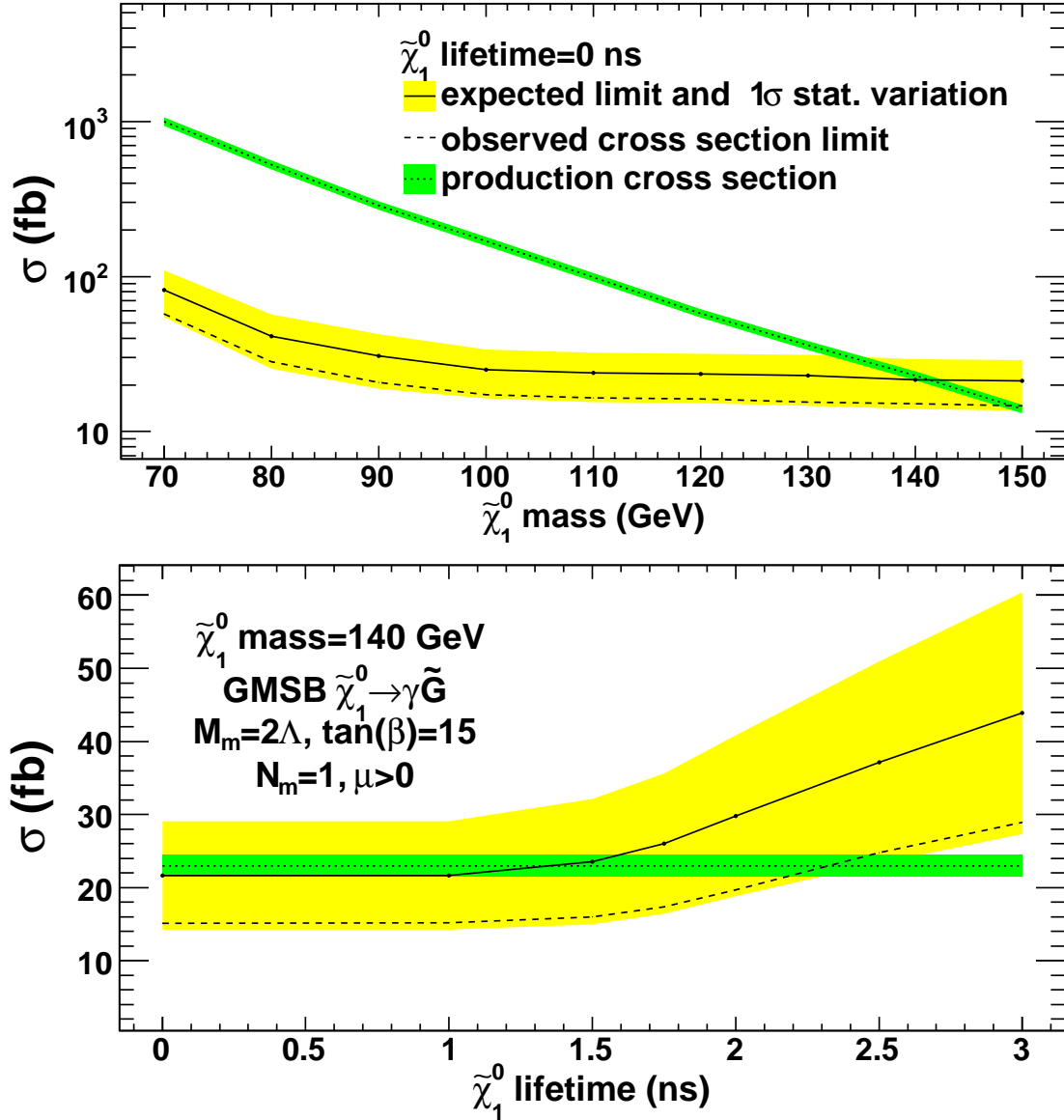


Figure 19: The predicted and observed cross section limits as a function of the $\tilde{\chi}_1^0$ mass at a lifetime of 0 ns (top) and as a function of the $\tilde{\chi}_1^0$ lifetime at a mass of $140 \text{ GeV}/c^2$ (bottom). Indicated in green is the 8.0% uncertainty-band for the production cross section, in yellow the RMS variation in the expected on the cross section limit.

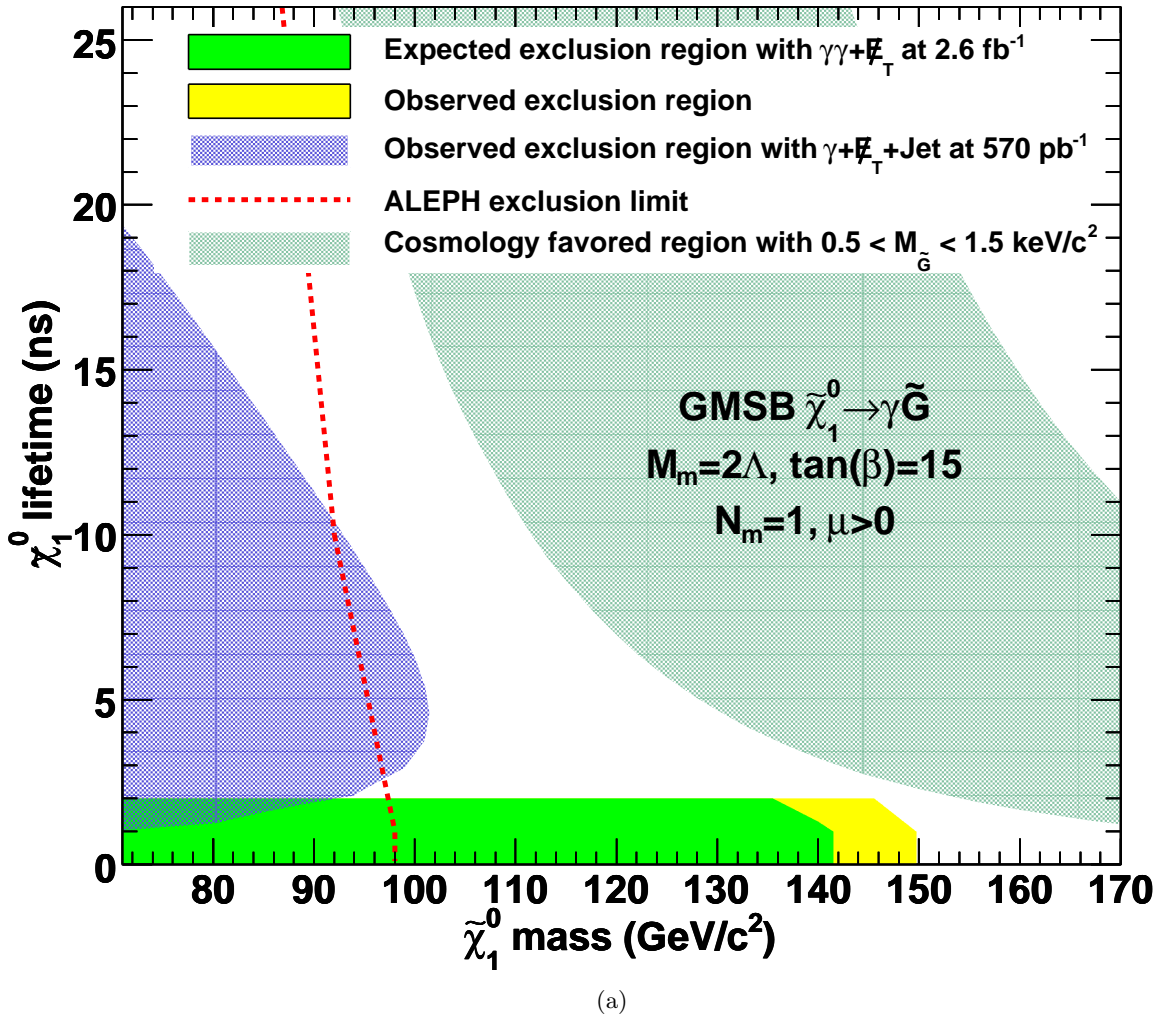


Figure 20: The predicted and observed exclusion region along with the limit from ALEPH/LEP [16] and the $\gamma + \cancel{E}_T + \text{jet}$ delayed photon analysis [19]. We have a mass reach of $141 \text{ GeV}/c^2$ (predicted) and $149 \text{ GeV}/c^2$ (observed) at the lifetime up to 1 ns. The blue shaded band shows the parameter space where $0.5 < m_{\tilde{G}} < 1.5 \text{ keV}/c^2$, favored in cosmologically consistent models [4].

C Appendix-III: Details of Large fake \cancel{E}_T from Pathologies

Instead of separating QCD backgrounds into two different categories as described in Sections 3.2.1 and 3.2.2 we can separate our QCD backgrounds into three types: 1) the standard energy mis-measurements (the *Met Model* prediction), 2) fake \cancel{E}_T from picking the wrong vertex in events where true collision did not create a vertex with no vertex ($N_{\text{signal}}^{\text{noVX}}$) and 3) tri-photon events with a lost photon that creates the fake \cancel{E}_T ($N_{\text{signal}}^{\text{TRI}}$). In this case the total QCD background prediction in the signal region, $N_{\text{signal}}^{\text{QCD}}$ is given by

$$N_{\text{signal}}^{\text{QCD}} = N_{\text{signal}}^{\text{MetModel}} + N_{\text{signal}}^{\text{noVX}} + N_{\text{signal}}^{\text{TRI}}. \quad (23)$$

In this section we describe last two categories for cross check.

C.1 Fake \cancel{E}_T from Picking the Wrong Vertex

To obtain a prediction for this background contribution, we model it using a PYTHIA $\gamma\gamma$ sample, “cdfpstn:gx0s1g”, with large statistics. Then we select PYTHIA $\gamma\gamma$ events that pass the kinematic cuts, including the \cancel{E}_T *Significance* cuts, but where the hard interaction does not produce a vertex, and the primary vertex is due to an overlapping Min-Bias interaction ($N_{\text{signal}}^{\text{noVX-MC}}$). To avoid double counting the number of events from energy mis-measurements with no vertex predicted by *Met Model* ($N_{\text{signal}}^{\text{noVX-MM-MC}}$) as described in Section 3.2.1, the final prediction of the wrong vertex background is given by

$$N_{\text{signal}}^{\text{noVX}} = (N_{\text{signal}}^{\text{noVX-MC}} - N_{\text{signal}}^{\text{noVX-MM-MC}}) \cdot \text{SF}_{\text{QCD}} \quad (24)$$

where SF_{QCD} is the same scale factor to normalize the MC sample to the data in Section 3.2.2.

The expected \cancel{E}_T , \cancel{E}_T *Significance*, H_T and $\Delta\phi(\gamma_1, \gamma_2)$ distributions are shown in Figure 21 for the sample of no vertex, MC events passing the preselection cuts.

The systematic uncertainties on this background prediction include the uncertainty on the scale factor and the uncertainty due to MC-data differences in the unclustered energy parameterization and the jet energy scale. To get the systematic uncertainty on the unclustered energy parametrization from the *Met Model* we deviate the default set of parameters by $\pm\sigma$. For the systematic uncertainty on the jet energy scale we follow the standard procedure at CDF [34]. The total uncertainty is estimated by adding the statistical uncertainty and these systematic uncertainties in quadrature.

C.2 Tri-Photon Events with a Lost Photon

To estimate this background, we use the exactly same strategy as in the wrong vertex background estimation. We select reconstructed tri-photon candidate events matched to HEPG level (generator level before detector simulation) photons ($E_T^{\gamma 1,2,3} > 13$ GeV) in the PYTHIA $\gamma\gamma$ sample and apply the kinematic cuts to these events, and multiply the result ($N_{\text{signal}}^{\text{TRI-MC}}$) by the same QCD scale factor, SF_{QCD} . Also, to avoid double counting the number of events from energy mis-measurements predicted by *Met Model* ($N_{\text{signal}}^{\text{TRI-MM-MC}}$) also as described in Section 3.2.1, the final prediction of the tri-photon background is given by

$$N_{\text{signal}}^{\text{TRI}} = (N_{\text{signal}}^{\text{TRI-MC}} - N_{\text{signal}}^{\text{TRI-MM-MC}}) \cdot \text{SF}_{\text{QCD}}. \quad (25)$$

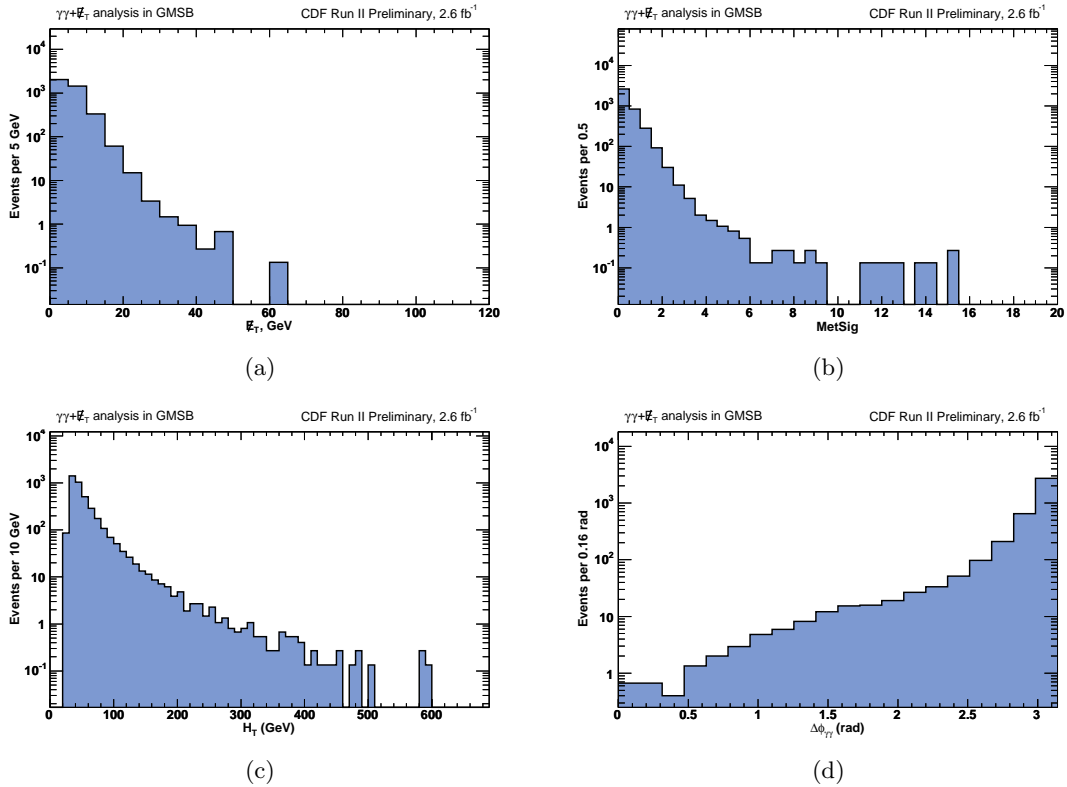


Figure 21: The QCD background from the 28,999 wrong vertex events with no vertex in the MC after the preselection requirements, but normalized by the SF_{QCD} scale factor. (a), (b), (c), and (d) show the \cancel{E}_T , \cancel{E}_T *Significance*, H_T , and $\Delta\phi(\gamma_1, \gamma_2)$ distributions respectively. The tails in \cancel{E}_T *Significance* are long, but the overall rate of this process is low.

The expected \cancel{E}_T , \cancel{E}_T *Significance*, H_T and $\Delta\phi(\gamma_1, \gamma_2)$ distributions are shown in Figure 22 for the sample of tri-photon, MC events passing the preselection cuts.

The systematic uncertainties on this background prediction also include the uncertainty on the scale factor and the uncertainty due to MC-data difference in the unclustered energy parameterization and the jet energy scale as in the wrong vertex background estimation. The total uncertainty is obtained by adding the statistical uncertainty and these systematic uncertainties in quadrature.

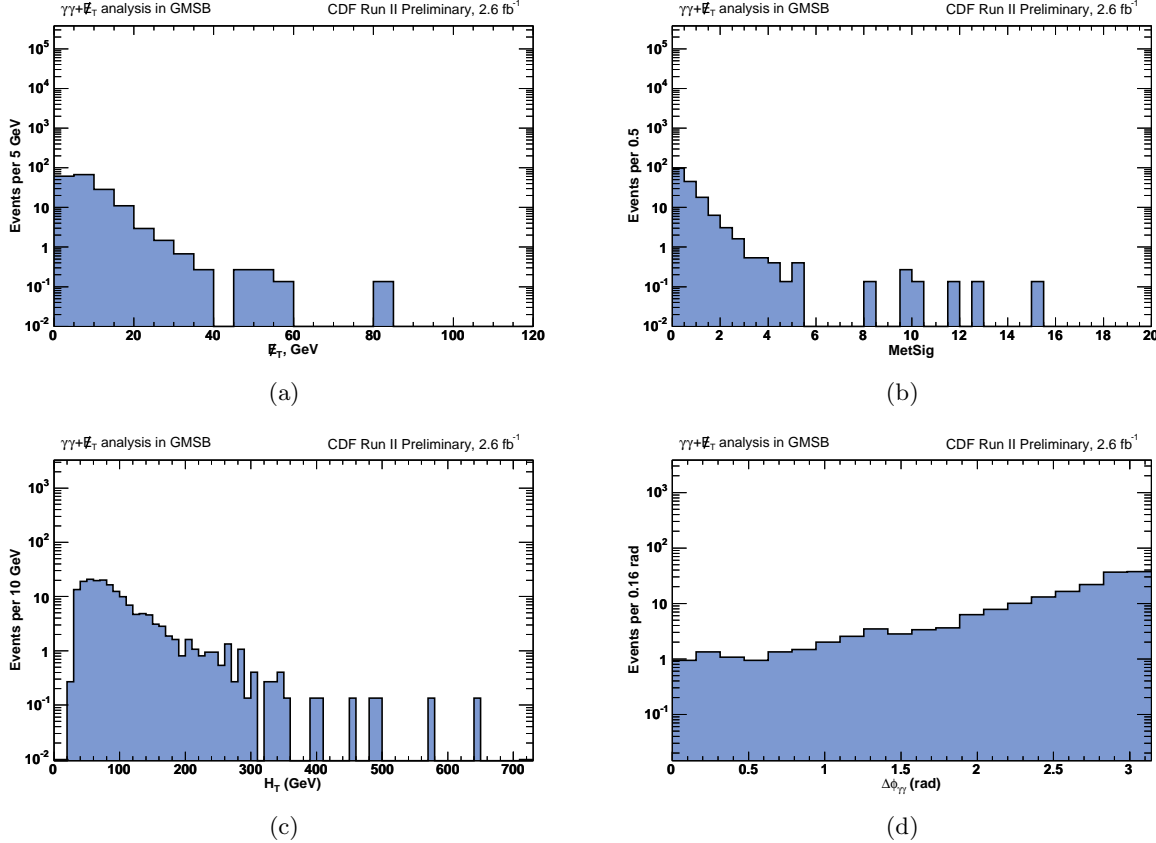


Figure 22: The QCD background from the 1,300 tri-photon events in the MC after the preselection requirements, but normalized by the SF_{QCD} scale factor. (a), (b), (c), and (d) show the \cancel{E}_T , \cancel{E}_T *Significance*, H_T , and $\Delta\phi(\gamma_1, \gamma_2)$ distributions respectively. The tails in \cancel{E}_T *Significance* are long, but the overall rate of this process is low.

After estimating all classes of QCD backgrounds, the expected kinematic distributions for the combined QCD sources after the preselection requirements are shown in Figure 23

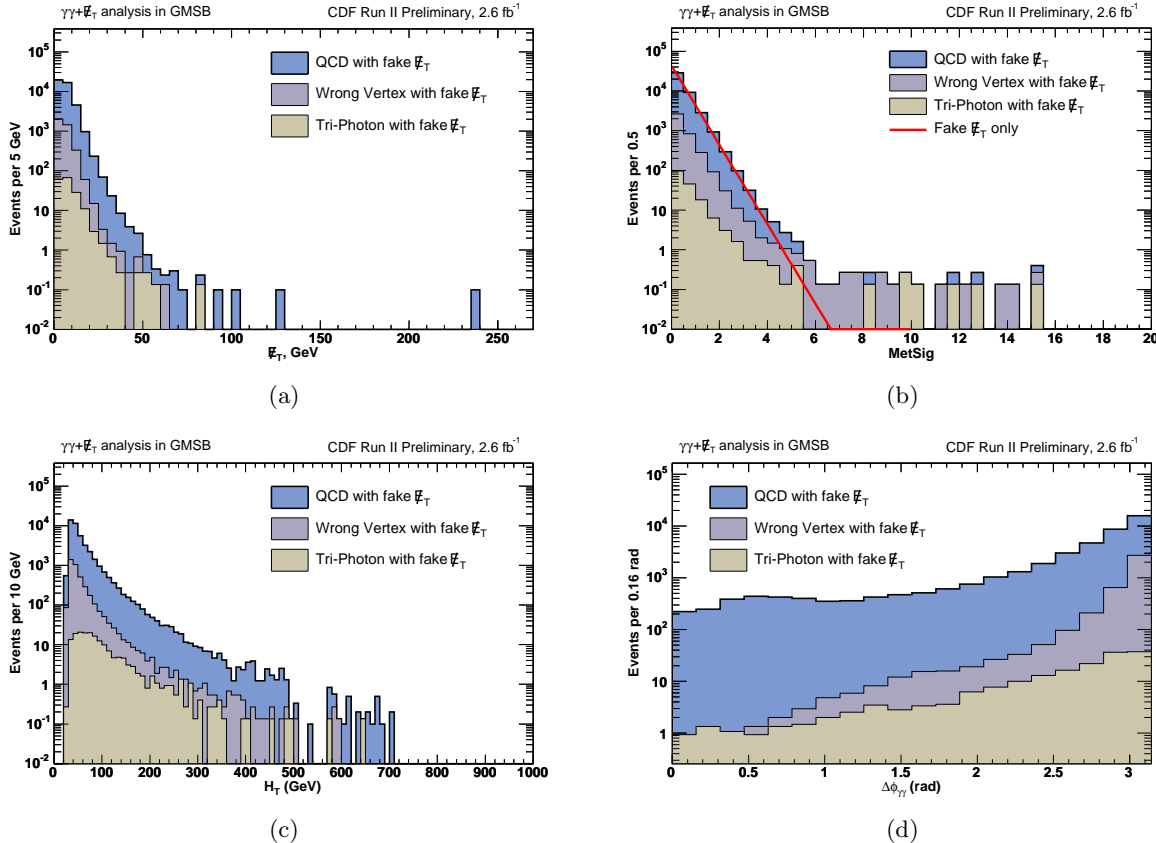


Figure 23: The combined QCD background predictions after the preselection requirements. (a), (b), (c) and (d) show \cancel{E}_T , \cancel{E}_T Significance, H_T and $\Delta\phi(\gamma_1, \gamma_2)$ distributions respectively. The red solid line in (b) shows the perfect prediction of fake \cancel{E}_T from energy mismeasurements only having no intrinsic \cancel{E}_T . In this case, the perfect prediction of \cancel{E}_T Significance has a simple *a priori* distribution of $dN/dx = N_{\text{event}} \times \ln(10) \times 10^{-x}$.

References

- [1] See for example, F. Halzen and A. D. Martin, “Quarks and Leptons,” John Wiley & Sons, 1984; C. Quigg, “Gauge Theories of the Strong, Weak, and Electromagnetic Interactions,” Addison-Wesley, 1983; and I. S. Hughes, “Elementary particles,” Cambridge University Press, 1990.
- [2] See for example S. Ambrosanio, G. L. Kane, G. D. Kribs, S. P. Martin and S. Mrenna, Phys. Rev. D **54**, 5395 (1996) or C. H. Chen and J. F. Gunion, Phys. Rev. D **58**, 075005 (1998).
- [3] H. Baer *et al.*, FERMILAB-Pub-00/251-T, S. Dimopoulos *et al.*, SLAC-PUB-7236 (1996).
- [4] J. L. Feng and T. Moroi, Phys. Rev. D **70**, 075019 (2004).
- [5] P. Bode, J. Ostriker and N. Turok, Astrophys. J. **556**, 93 (2001).
- [6] CDF Collaboration, F. Abe *et al.*, Phys. Rev. Lett. **81**, 1791 (1998); Phys. Rev. D **59**, 092002 (1999).
- [7] P. Wagner and D. Toback, Phys. Rev. D **70**, 114032 (2004).
- [8] M. Goncharov, V. Krutelyov, E. Lee, D. Toback, and P. Wagner, “Search for Heavy, Neutral, Long-Lived Particles that Decay to Photons”, CDF Note 8016.
- [9] In progress.
- [10] B. C. Allanach *et. al.*, Eur. Phys. J. C**25**, 113 (2002).
- [11] PYTHIA: T. Sjöstrand, L. Lönnblad and S. Mrenna, arXiv:hep-ph/0108264 (2001); *cdfsoft* 6.1.2 has PYTHIA version 6.216. *cdfSim*: G.S. Sganos, Tutorial on *cdfSim*. We modified it for the simulation of the EMTiming system [36]. It further includes a bug-fix of the tracking code to simulate the CES response to photons from displaced vertices correctly and a patch by A. Scott to include decay products of displaced $\tilde{\chi}_1^0$ in the detector simulation [37].
- [12] W. Beenakker, *et al.*, Phys. Rev. Lett. **83**, 3780 (1999).
- [13] P. Simeon and D. Toback, “An Advantage of Setting Cross Section Limits on the Total Production Mechanism When Multiple Processes Produce the Same Final State,” CDF Note 7084 (2006).
- [14] The remaining processes produce slepton pairs that also decay to pairs of $\tilde{\chi}_1^0$: τ_1 ($\sim 9\%$), e_R ($\sim 7\%$), μ_R ($\sim 7\%$).
- [15] DØ Collaboration, B. Abbott *et. al.*, Phys. Rev. Lett. **80**, 442 (1998).
- [16] ALEPH Collaboration, A. Heister *et. al.*, Eur. Phys. J. C **25**, 339 (2002); A. Garcia-Bellido, Ph.D. thesis, Royal Holloway University of London (2002) (unpublished), arXiv:hep-ex/0212024.
- [17] CDF Collaboration, D. Acosta *et. al.*, Phys. Rev. D **71**, 031104 (2005).
- [18] DØ Collaboration, V.M. Abazov *et. al.*, Phys. Lett. B **659**, 856 (2008).
- [19] CDF Collaboration, A. Abdulencia *et. al.*, Phys. Rev. Lett **99**, 121801 (2007); CDF Collaboration, T. Aaltonen *et. al.*, Phys. Rev. D **78**, 032015 (2008).

- [20] M. Goncharov *et. al.*, “The Timing System for the CDF Electromagnetic Calorimeters,” CDF Note 7918 (2005), NIM **A565**, 543 (2006).
- [21] R. Culbertson, M. Goncharov, and A. Pronko, “Search for Anomalous Production of $\gamma\gamma + \cancel{E}_T$ Events in 2 fb^{-1} of Data”, CDF Note 9184.
- [22] S. Jindariani *et al.*, “Luminosity Uncertainty for Run 2 up until August 2004”, CDF Note 7446.
- [23] <http://www-cdf.fnal.gov/internal/physics/photon/goodrun.html>, file goodrun_v17_ph0_02.txt.
- [24] <http://www-cdf.fnal.gov/internal/dqm/goodrun/good.html>, the script SAMLumi.ksh to compute luminosities for a given goorun list and dataset.
- [25] Ray Culbertson *et al.*, “Search for Anomalous $\gamma\gamma + \cancel{E}_T$ Production and Limits on GMSB Models”, CDF Note 6389.
- [26] S-M Wynne, T. Berry, and R. Culbertson, “ID Efficiencies for Very High-Pt Photons”, CDF Note 8302. For MC simulation the efficiency of the χ^2_{CES} starts falling off at 100 GeV and starts dipping pretty seriously. However, the MC simulation is not accurate so it is more true that we just do not know what the efficiency is above the E_T scale of the Z events, where we can check it in data.
- [27] http://www-cdf.fnal.gov/tiki/tiki-index.php?page_ref_id=57, Stntuple dev_243 build instructions.
- [28] P. Onyisi, “Run 2 gamma+met search”, CDF Note 6381.
- [29] CDF Collaboration, F. Abe *et al.*, Phys. Rev. Lett. **52**, 4784 (1995).
- [30] R. Culbertson, A. Pronko, and Shin-Shan Eiko Yu, “The Probability of an Electron Faking an Isolated Prompt Photon in CEM”, CDF Note 8220.
- [31] M. Goncharov *et al.*, “Methods for Determining the Photon Event Rates and Timing Distributions for Searches with Final State Photons”, CDF Note 7960.
- [32] M. Goncharov *et al.*, “Discrimination of Beam Halo and Cosmic Rays as a Source of Photon Candidates”, CDF Note 8409.
- [33] CDF Collaboration, F. Abe *et al.*, Phys. Rev. Lett. **81**, 1791 (1998).
- [34] <http://www-cdf.fnal.gov/internal/physics/top/jets/systematics.html>
- [35] http://www-cdf.fnal.gov/physics/ewk/mc_samples.html
- [36] M. Goncharov, V. Krutelyov, D. Toback and P. Wagner, “Resolution and Simulation of the EMTiming System”, CDF Note 7928 (2006).
- [37] M. Goncharov, D. Toback and P. Wagner, “Identification Efficiencies for Photons from Heavy, Long-Lived, Neutral Particles”, CDF Note 7929 (2006).
- [38] The ISASUGRA output is converted to PYTHIA using a script by A. Scott.

- [39] R. Rossin, CDF Detector Lectures: “Systematics on the Luminosity Measurement”, http://fcdfwww.fnal.gov/internal/WebTalks/Archive/0410/041007_clclum_detector_lecture/04_041007_clclum_detector_lecture_Roberto_Rossin_1_RobertoCLC_detector-04-10-07.pdf; S. Klimenko, J. Konigsberg and T. M. Liss, FERMILAB-FN-0741 (2003).
- [40] C. Group, R. Culbertson, and J. Ray, “Photon Efficiency Scale Factor”, CDF Note 9429 (2008).
- [41] M. McFarlane, H. Bachacou, J. Nielsen, and W. Yao, “Study of High p_T Lepton Identification Efficiency Scale Factor and Related Cuts and Parameters in 5.3.3”, CDF Note 7682 (2005).
- [42] http://www-cdf.fnal.gov/internal/physics/joint_physics/agenda/20050527-minutes.html
- [43] O. Gonzalez and C. Rott, “Uncertainties due to the PDFs for the gluino-sbottom search”, CDF Note 7051 (2005).
- [44] M. Griffiths *et. al.*, “Searches for Chargino and Neutralino in the $e+e/\mu+\mu$ with 1 fb-1 of data”, CDF Note 8389 (2006).
- [45] see e.g. W. Beenakker, *et al.*, Nucl. phys. B **492**, 51 (1997); Prospino 2.0: <http://www.ph.ed.ac.uk/~tlehn/prospino/prospino.html>
- [46] E. Boos, A. Vologdin, D. Toback and J. Gaspard, Phys. Rev. D **66**, 013011 (2002). J. Conway, CERN Yellow Book Report No. CERN 2000-005 (2000), p. 247.